Theoretical Prediction of Dynamic Composite Material Properties for Hypervelocity Impact Simulations

S. Ryan, M. Wicklein, A. Mouritz, W. Riedel, F. Schäfer, K. Thoma

To cite this version:

S. Ryan, M. Wicklein, A. Mouritz, W. Riedel, F. Schäfer, et al.. Theoretical Prediction of Dynamic Composite Material Properties for Hypervelocity Impact Simulations. International Journal of Impact Engineering, 2009, 36 (7), pp.899. 10.1016/j.ijimpeng.2008.12.012 . hal-00574818

HAL Id: hal-00574818

https://hal.science/hal-00574818

Submitted on 9 Mar 2011

Accepted Manuscript

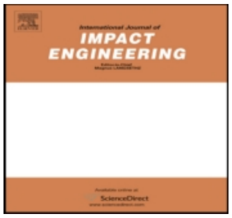

Title: Theoretical Prediction of Dynamic Composite Material Properties for Hypervelocity Impact Simulations

Authors: S. Ryan, M. Wicklein, A. Mouritz, W. Riedel, F. Schäfer, K. Thoma

PII: S0734-743X(08)00329-1
DOI: 10.1016/j.ijimpeng.2008.12.012
Reference: IE 1740

To appear in: *International Journal of Impact Engineering*

Received Date: 29 July 2008
Revised Date: 3 December 2008
Accepted Date: 17 December 2008

Please cite this article as: Ryan S, Wicklein M, Mouritz A, Riedel W, Schäfer F, Thoma K. Theoretical Prediction of Dynamic Composite Material Properties for Hypervelocity Impact Simulations, International Journal of Impact Engineering (2009), doi: 10.1016/j.ijimpeng.2008.12.012

Theoretical Prediction of Dynamic Composite Material Properties for Hypervelocity Impact Simulations

S. Ryan[1,2], M. Wicklein[1], A. Mouritz[2], W. Riedel[1], F. Schäfer[1], K. Thoma[1]

[1]Fraunhofer-Institute for High-Speed Dynamics, FhG Ernst-Mach-Institute (EMI), Germany
[2]School of Aerospace, Mechanical & Manufacturing Engineering, RMIT University, GPO Box 2476V, Melbourne, Australia

Abstract

Recent advances in the description of fibre-reinforced polymer composite material behaviour under extreme loading rates provide a significant extension in capabilities for numerical simulation of hypervelocity impact on composite satellite structures. Given the complexity of the material model, extensive material characterisation is required, however, as the properties of composite materials are commonly tailored for a specific application, experimental characterisation is not efficient, particularly in preliminary design phases. As such, a procedure is outlined in this paper that applies a number of commonly accepted composite mechanics and shock physics theories in conjunction with generalised material properties which allows for the theoretical derivation of a complete material data set for utilisation of the new modelling capabilities. The derivation procedure has been applied to a carbon fibre/epoxy laminate, and is validated through a comparison of derived material properties with experimentally-characterised values and numerical simulation of damage induced by hypervelocity impact on a representative space debris shielding configuration employing the CFRP laminate. For the specific structures and impact conditions considered, application of the material property derivation procedure in place of experimental characterisation provided comparable accuracy in the prediction of damage induced by particles impacting at hypervelocity.

Keywords: Hypervelocity impact; Orbital debris; Hydrocode; CFRP; Numerical simulation

1 Introduction

Since 1957 over 4,000 successful launches by the international space community have deployed in excess of 17,000 objects in orbit about the Earth [1]. Ranging from derelict spacecraft and launch vehicle upper stages to paint flakes and solid rocket motor effluents, these launches have generated a current man-made debris population consisting of approximately 10,000 objects larger than 10 cm, 100,000 objects between 1 and 10 cm, and tens of millions of particles smaller than 1 cm. Although efforts are being undertaken to mitigate the generation of additional space debris (e.g. [2]), the pollution of key altitudes has already (in some cases) exceeded a critical density, i.e. even if no new launches were conducted, the number of debris objects will continue to uncontrollably increase as a result of collisions between existing debris bodies [3]. As such, the threat to operational spacecraft posed by the impact of space debris particles at hypervelocity continues to increase. Due to their potentially high speeds (e.g. from 11 to 72 km/s for meteoroids) and collision energies, the impact of space debris can be critical to mission safety. However, assessing the risk is difficult as only approximately 40% of impact conditions relevant for low-Earth orbiting (LEO) spacecraft can be experimentally reproduced. Numerical hydrocodes are commonly used in the support of experimental risk analysis programs as they are ideal for simulation of these highly dynamic, shockwave-inducing events (e.g. [4][5]). Furthermore, recent advances [6][7] in the modelling of composite materials provide an improvement over existing capabilities by allowing the macromechanical description of orthotropic constitutive behaviour, non-linear equation of state, orthotropic non-linear irreversible strain, and individual material plane interactive failure initiation criteria. Application of these new capabilities in modelling the hypervelocity impact of aluminium fragments on Aramid/epoxy plates [7] and aluminium projectiles on carbon fibre reinforced polymer (CFRP)/Aluminum honeycomb (HC) sandwich panels (SP) [8] has shown the ability to reproduce many of the damage phenomena observed in experiments.

In previous applications of the advanced orthotropic composite material model for analysing hypervelocity impact events (e.g. [7], [8]), material data has been determined through experimental characterisation programs. As the directional performance of a fibre-reinforced polymer can be altered through composition, orientation of the constituents, and fibre packing geometry, full experimental characterisation is required for each new material configuration. Subsequently, the time and expense involved in determination of accurate material data sets for application of the advanced composite material model can be prohibitive.

In this paper an analytical procedure is outlined that combines a number of shock physics and composite mechanics theories to derive a full set of material data for a space-representative

CFRP laminate. This procedure enables application of the advanced composite model in the simulation of hypervelocity impact on composite materials when experimental material characterisation is not viable. Although not intended to fully replace the need for experimental characterisation, the analysis procedure provides a means of performing material sensitivity studies in the first phase of satellite structural design that allows the quick and cost-effective comparison of the debris shielding performance of competing material configurations.

2 Advanced Orthotropic Composite Continuum Material Model

A new material model for composite materials was derived by Riedel and Clegg et al. [6][7] to address material anisotropy, shock response and anisotropic strength degradation (damage) under impact loading. Key aspects of the model are reviewed herein.

2.1 Modelling basic orthotropic stiffness and shock response

A shock wave can be defined as a discontinuity in pressure, P, temperature (or internal energy, E) and density, ρ. Therefore, in the analysis of shock wave propagation within a continuum, and its effect on the continuum properties, equations are developed by considering regions immediately ahead (reference condition indicated by the subscript 0) and behind an infinitely thin shock. The conservation laws across a shock front were originally defined by Rankine and Hugoniot for fluids, and are defined as:

Conservation of mass:

$$\rho_0 U_s = \rho(U_s - u_p) \tag{1}$$

Conservation of momentum:

$$(p - p_0) = \rho_0 U_s u_p \tag{2}$$

Conservation of energy:

$$E - E_0 = \frac{1}{2}(p + p_0)(V_0 - V) \tag{3}$$

where: $V = \frac{1}{\rho}$ U_s – shock velocity u_p – particle velocity

The Equation of State (EOS) is required to solve the conservation equations. For isotropic solid continua, the EOS is commonly expressed in the Mie-Grüneisen form:

$$p = p_r(v) + \frac{\Gamma(v)}{v}\left[E - E_r(v)\right] \tag{4}$$

where Γ is the Grüneisen gamma: $\Gamma(v) = v\left(\frac{\partial p}{\partial E}\right)_v$

The functions $p_r(v)$ and $E_r(v)$ refer to the internal pressure and energy of the compressed material in terms of volume, and are generally known functions on some reference curve. For example, with the Hugoniot as reference:

$$p - p_H = \Gamma\rho\left(E - E_H\right) \tag{5}$$

The Mie-Grüneisen formulation of the hydrodynamic EOS describes the thermodynamic response of a material under shock loading (i.e. the material behaves like a gas or fluid, having no strength). During hypervelocity impact, pressures are generated that can exceed the strengths of impacting materials (projectile, target) by orders of magnitude [9], thus the materials are effectively behaving hydrodynamically. However, there exist two regimes – far field and late time – where strength effects may be important. As the impact-induced stresses decrease with distance from the impact location, there may be far-field regions in the target where local stress levels are of the order of material strength or lower. Furthermore, as the projectile is slowed within the target the impact-induced stresses will also decrease. If the target is sufficiently thick, the stresses may decrease to the level of magnitude (or lower) of the material strength. Description of the strength effects under shock loading is referred to as constitutive modelling. Historically, the thermodynamic (EOS) response of a material and its ability to carry shear loads (strength) were dealt with separately by partitioning the strain into volumetric and deviatoric components. However, for anisotropic materials this approach is unsuitable, as (from [10]):

- Strain is not uniform in all three (principal) directions under hydrostatic pressure, and;
- Deviatoric strain will produce volumetric dilation since the coefficients in the stress/strain relation are not all equal.

A new formulation of the EOS for composite materials that provides a coupled deviatoric and volumetric response was derived by Anderson et al. [10] and takes the form:

$$p = p_H - \Gamma\rho\left(E - E_H\right) - \frac{1}{3}\left[C_{11} + C_{21} + C_{31}\right]\varepsilon_{11}^d - \frac{1}{3}\left[C_{12} + C_{22} + C_{32}\right]\varepsilon_{22}^d - \frac{1}{3}\left[C_{13} + C_{23} + C_{33}\right]\varepsilon_{33}^d \tag{6}$$

where ε_{ii}^d - deviatoric strain component
C_{ij} - terms of the orthotropic stiffness matrix

The volumetric portion of Eq. (6) can be expressed by a polynomial formulation of the Mie-Grüneisen EOS:

$$p = K_1\mu + K_2\mu^2 + K_3\mu^3 + \left(B_0 + B_1\mu\right)\rho_0 E \qquad (7)$$

where μ – volumetric strain = $\dfrac{\rho}{\rho_0} - 1$

K_i and B_i are material constants which can be defined separately for compression and expansion, i.e.:

For $\mu > 0$ (compression):

$$p = A_1\mu + A_2\mu^2 + A_3\mu^3 + \left(B_0 + B_1\mu\right)\rho_0 E \qquad (8)$$

For $\mu < 0$ (tension):

$$p = T_1\mu + T_2\mu^2 + B_0\rho_0 E \qquad (9)$$

The polynomial formulation of μ in Eq. (8)-(9) is an alternate means of describing the Hugoniot pressure, p_H. The material constants K_i must then be correlated with the Hugoniot parameters in order to approximate the values of the shocked material parameters. In the case of a material with a linear shock velocity-particle velocity relationship (i.e. Hugoniot curve in the U_s-u_p plane), the parameters K_i of the polynomial relationship can be calculated using:

$$K_1 = \rho_0 {c_B}^2 \qquad (10)$$

$$K_2 = \rho_0 {c_B}^2 \left[1 + S\left(S - 1\right)\right] \qquad (11)$$

$$K_3 = \rho_0 {c_B}^2 \left[2\left(S - 1\right) + 3\left(S - 1\right)^2\right] \qquad (12)$$

For an isotropic Hookean material, Eq. (10) is equivalent to a linear EOS, where K_1 represents the bulk modulus of the material. For an anisotropic material, to ensure consistency in the elastic regime, the bulk modulus is considered as an “effective” or “average” bulk modulus K_1' and is defined from the orthotropic stiffness matrix [C]:

$$A_1' = \frac{1}{9}\left[C_{11} + C_{22} + C_{33} + 2\left(C_{12} + C_{13} + C_{23}\right)\right] \qquad (13)$$

The second part of the polynomial expression (Eq. (7)) is associated with shock conditions located off the Hugoniot curve and is formulated using two parameters to distinguish the density dependence of the Grüneisen gamma, Γ, where:

$$\Gamma = \frac{B_0 + B_1\mu}{1+\mu} \tag{14}$$

and Γ = constant for $B_0 = B_1$ $\Gamma\rho$ = constant for $B_1 = 0$ Γ is linear in ρ for $B_0 \neq B_1 \neq 0$

2.2 Modelling irreversible, non-linear damage

Chen et al. [11] derived a three-dimensional (3D) quadratic yield stress function which relaxes the constant pressure assumption of the Tsai-Hill anisotropic yield criterion, allowing a change in volume (and thus pressure) contribution from deviatoric strain. The yield function includes a hardening parameter to describe increasing strength with increasing plastic deformation. The quadratic yield function is expressed as:

$$\begin{aligned} f\left(\sigma_{ij}\right) = a_{11}\sigma_{11}^2 + a_{22}\sigma_{22}^2 + a_{33}\sigma_{33}^2 + 2a_{12}\sigma_{11}\sigma_{22} + 2a_{23}\sigma_{22}\sigma_{33} + \ldots \\ 2a_{13}\sigma_{11}\sigma_{33} + 2a_{44}\sigma_{23}^2 + 2a_{55}\sigma_{31}^2 + 2a_{66}\sigma_{12}^2 = k \end{aligned} \tag{15}$$

The nine a_{ij} coefficients are referred to as plasticity coefficients, and are used to describe the amount of anisotropy in plasticity, while *k* is a state variable defining the instantaneous value of the limit surface. In the quadratic yield function a so-called *master effective stress-effective strain curve* is defined. The nine plasticity coefficients are then capable of collapsing specific loading conditions onto the master curve, and thus the plasticity of an orthotropic laminate in any 3D loading case can be determined.

2.3 Modelling failure initiation

For impact loading on reinforced composite materials, the dominant modes of damage are: delamination caused by through thickness strain, shear strain causing matrix cracking, and fibre failure. These damage modes lead to a reduction in the load carrying capability of the material, which is referred to as softening. To account for the anisotropic nature of these damage modes, modified forms of the well-known Hashin criteria which include out-of-plane shear stresses for fibre failure and matrix cracking are used to evaluate failure initiation [12]:

$$e_{iif}^2 = \left(\frac{\sigma_{ii}}{\sigma_{ii,u}}\right)^2 + \left(\frac{\sigma_{ij}}{\sigma_{ij,u}}\right)^2 + \left(\frac{\sigma_{ki}}{\sigma_{ki,u}}\right)^2 \geq 1 \tag{16}$$

NOTE: Initiation criteria only applied in tension

If one of the failure criteria are exceeded ($e_{iif}^{2} > 1$), the orthotropic post-failure softening model is activated.

2.4 Modelling non-linear softening

When the state of stress is calculated to lie outside the limit surface defined by Eq. (16) an inelastic strain increment is accumulated as crack strain, ε_{cr}. The maximum stress that can be sustained by the laminate is reduced as a function of crack strain (damage), according to:

$$\sigma_u = \sigma_{fail}\left(1 - Dam\right) \tag{17}$$

where $$Dam_{ij} = \left(\frac{L_{ij}F_{ij}^{2}}{2G_{ij}^{f}}\right)\left(\frac{\varepsilon_{ij}^{cr}}{F_{ij}}\right)$$

and F_{ij}^{2} is the initial failure stress in the three material directions (kPa)

G_{ij}^{f} is the fracture energy for each mode of failure (J)

L_{ij} is the characteristic cell dimension in the direction of failure

3 Derivation of Material Parameters for Application in the Advanced Orthotropic Composite Continuum Material Model

An experimental program (described in [8]) was used to characterise the properties of a space-representative CFRP laminate for implementation in the advanced orthotropic composite material model. Details of the laminate are given in Table 1. In the following section, the theoretical procedure for derivation of CFRP dynamic properties is applied to this laminate.

Table 1 Properties of the CFRP laminate subject to characterisation

Property	*Value / Description*
Fibre type	Tenax UMS2526
Resin type	Krempel BD System 120°C epoxy resin
Fibre volume content	52 %
Lay-up	[0/45/-45/-45/45/0]
Thickness	1.37 mm

3.1 Characterising basic orthotropic stiffness and shock response

3.1.1 Basic orthotropic stiffness

In the absence of manufacturer-supplied material data, constituent (fibre and matrix) product data sheets represent a starting point for derivation of composite laminate mechanical properties. Micromechanical theories can generally be classified into elastic or strength theories. Although no single elastic or strength theory receives universal application, the accuracy of micromechanics for predicting the elastic properties of composite lamina is widely accepted. To identify the elastic micromechanics theory best suited for predicting the properties of space-grade CFRP composite laminates, six of the most common theories are subject to a critical review: mechanics of materials [13]; semi-empirical approach [14]; self-consistent field [15]; equivalent inclusion method [16]; method of cells [17], and; bridging method [18].

The critical review is performed by evaluating the predictions of the six theories for three freely available carbon fibre/epoxy composite material data sets: IM6/3501-6 (V_f = 63.5%) [19], T300/BSL914C (V_f = 60%) [20], and AS4/3501-6 (V_f = 60%) [20]. The variance of the micromechanics predictions from the measured values is shown in Figure 1. For the longitudinal tensile modulus (E_{11}) and major Poisson's ratio (ν_{12}) the various methods (with the exception of Method of Cells) all predict an effectively identical result which is within 10% of the reported value for the three composites. It appears that the predictive accuracy of the six micromechanics theories is dependent on the material data sets. For example, the transverse tensile modulii (E_{22}) of AS4/3501-6 and T300/BSL914C are significantly under-predicted, however for the IM6/3501-6 material the predictions are reasonably accurate.

The accuracy of the six micromechanics theories for predicting the elastic properties of the three carbon/epoxy composites considered is assessed in two ways: 1) a direct calculation of the average error (%), and; 2) a Rule of Measure (ROM) which ranks the theories according to their prediction for each elastic property of each material. In each case, the theories are ranked from best to worst and assigned a score ranging from 1 (best) to 6 (worse). A summary of the accuracy evaluation is given in Table 2. With both evaluation methods Huang's bridging method provides the best overall agreement with the reported quasi-static composite material propeties.

Table 2 Evaluating the predictive accuracy of six micromechanics theories for three CFRP materials.

	Ave. % error		ROM total	
Theory	Value	Rank	Value	Rank
Mech. of materials	11.5	3	66	5
Semi-empirical	11.6	4	63	4
Self-consistent field	10.9	2	75	6
Equivalent incl.	11.8	5	61	2
Method of cells	14.4	6	62	3
Bridging method	10.2	1	51	1

Once the elastic properties of the composite material are known, Classical Laminate Theory (CLT) provides the means to determine the elastic behaviour of composite laminates within the framework of the following assumptions:

- Each ply in the laminate is quasi-homogenous and orthotropic;
- The laminate is thin with lateral dimensions much larger than its thickness;
- The laminate is loaded in a state of plane stress (i.e. $\sigma_z = \tau_{xz} = \tau_{yz} = 0$);
- There is no transverse shear.

CLT assumes a state of plane stress to enable derivation of the in-plane properties without the need for consideration of the through-thickness behaviour of the laminate. To derive the laminate out-of-plane properties, Hooke's law for an orthotropic composite can be used as it uses a transformation matrix which is a factor of the stress tensor (and therefore considers through-thickness effects), i.e.:

For plane stress (CLT),

$$[\sigma] = \begin{bmatrix} \sigma_1 \\ \sigma_2 \\ \sigma_6 \end{bmatrix} \quad \text{or in body-coordinate system} \quad [\sigma] = \begin{bmatrix} \sigma_{xx} \\ \sigma_{yy} \\ \sigma_{xy} \end{bmatrix} \tag{18}$$

For two-dimensional stress-tensor (Hooke's law),

$$[\sigma] = \begin{bmatrix} \sigma_1 \\ \sigma_2 \\ \sigma_3 \\ \sigma_4 \\ \sigma_5 \\ \sigma_6 \end{bmatrix} \quad \text{or in body-coordinate system} \quad [\sigma] = \begin{bmatrix} \sigma_{xx} \\ \sigma_{yy} \\ \sigma_{zz} \\ \sigma_{yz} \\ \sigma_{xz} \\ \sigma_{xy} \end{bmatrix} \tag{19}$$

For symmetric laminates no coupling exists between in-plane loading and out-of-plane deformation, i.e. no flexural/twisting moments are produced under in-plane loading. In this case the laminate stiffness matrix, C, can be determined simply by summing the contributions of each ply in terms of their respective thickness, i.e.:

$$C_{ij} = \sum_{k=1}^{n} C_{ij,k} \times \frac{t_{ply,k}}{t_{lam}} \tag{20}$$

where k – individual ply index
n – total number of plies
$t_{ply,k}$ – thickness of ply k
t_{lam} – total thickness of the laminate

For the UMS2526/Krempel BD laminate defined in Table 1, the orthotropic stiffness properties have been calculated using constituent properties listed in Table 3 with the micromechanical bridging model, CLT, and Hooke's law. The calculated properties (see Table 4) show reasonable agreement with experimentally characterised values, particularly the in-plane parameters. However, given the uncertainties in estimating unknown constituent properties, the agreement is considered good.

Table 3 Constituent properties for micromechanics

Property	*Value*	*Source*
Fibre:		
Density (ρ_f)	1.79 g/cm³	(a)
Long. tensile mod. (E_{f11})	395 GPa	(a)
Trans. tensile mod. (E_{f22})	13.33 GPa	(b)
Poisson's ratio (ν_{f12})	0.2385	(c)
Trans. Poisson's ratio (ν_{f23})	0.2981	(c)
Shear modulus (G_{f12})	24.80 GPa	(b)
Trans. shear modulus (G_{f23})	5.80 GPa	(d)
Long. tensile strength (X_{ft})	4560 MPa	(a)
Long. comp. strength (X_{fc})	2042 MPa	(c)
Resin:		
Density (ρ_m)	1.22 g/cm³	(a)
Tensile modulus (E_m)	3.10 GPa	(c)
Poisson's ratio (ν_m)	0.375	(c)
Shear modulus (G_m)	1.127 GPa	(d)
Tensile strength (X_{mt})	73.82 MPa	(c)
Compression strength (X_{mc})	280.4 MPa	(e)
Shear strength (S_{mxy})	86.63 MPa	(c)
Fracture energy (G_{fm})	240 J/m²	(c)

(a) Manufacturer data sheet
(b) Constituent relationship [21]
(c) Common / average property
(d) Isotropy / transverse isotropy
(e) 10 % rule [22]

Table 4 Theoretically and experimentally derived orthotropic stiffness properties of the UMS2526/Krempel BD laminate.

Parameter	*Theory*	*Exp.*
Reference density [g/cm^3]	1.516	1.563
Young's Modulus 11 [GPa]	79.24	72.90
Young's Modulus 22 [GPa]	30.25	22.89
Young's Modulus 33 [GPa]	8.71	9.07
Poisson's Ratio 12 []	0.84	0.77
Poisons Ratio 23 []	0.33	0.55
Poisson's Ratio 31 []	0.0071	0.0187
Shear Modulus 12 [GPa]	36.32	48.35
Shear Modulus 23 [GPa]	2.87	0.558
Shear Modulus 31 [GPa]	3.36	0.873

3.1.2 Shock response

The shock response of the CFRP laminate is defined by Eq. (6), incorporating a coupled deviatoric and volumetric strain response. The volumetric response (EOS) is expressed using a polynomial form of the Mie-Grüneisen EOS (Eq. (7)). In this case, it is assumed that shock response under compression and tension is the same, and therefore $A_1' = T_1$ and $A_2 = T_2$. Flyer plate impact tests on isotopic materials allow shock and particle velocity properties to be deduced, from which the reference curve (generally the Hugoniot) can be defined. However, as a result of the coupled strain response, these tests are not accurate for anisotropic materials and should only be used for validation of complete numerical models via a comparison of rear side velocity-time signals. A theory for the direct derivation of the coefficients in the polynomial equation EOS, coupled with orthotropic response, is currently not available. Nonetheless, flyer plate impact tests on orthotropic materials are commonly used for the definition of the Hugoniot reference curve (e.g. [23], [24]).

Three different CFRP laminates subjected to flyer plate impact tests (IM7/8552 [25], T800H/B413M15 [26], and UMS2526/Krempel BD [8]) showed a high level of similarity when normalised in terms of the material primary sound speed (c_p) at shock inducing impact velocities, as shown in Figure 2a. For particle velocities less than ~500 m/s, a plastic wave is induced which is expected to be dispersive as a result of plastic damage such as matrix cracking, delamination, etc. Continuous stress measurements have been made during PPI tests on mortar by Kawai et al. [27] which demonstrate the relationship between plastic damage and reduced wavespeed (dispersive plastic phase). It is considered that a similar phenomenon is measured in the CFRP samples, resulting in decreasing shock velocity measurements for increasing particle velocity below the onset of shock wave generation.

The p-wave soundspeed of the three laminates was measured via ultrasound as 3100 m/s, 2900 m/s, and 2800 m/s respectively. A linear best fit is made to the normalised experimental data (considering particle velocities above 500 m/s), shown in Figure 2a. The linear curve is defined as:

$$U_s = \left(6.242E-04 \cdot u_p + 6.707E-01\right) \cdot c_p \tag{21}$$

Using the generalised U_s-u_p relationship (Eq. (21)) and a measured p-wave soundspeed of 2800 m/s, the polynomial equation of state parameters for the UMS2526/Krempel BD CFRP laminate are calculated from Eq. (10)-(13). Additionally, the Grüneisen gamma is calculated using the approximation proposed in [28]:

$$B_0 = B_1 = \Gamma \cong 2S - 1 \tag{22}$$

A comparison with the experimentally-determined parameters is made in Table 5. The principle differences between the calculated and measured equation of state parameters lie in the quadratic and cubic compression modulii (A2, A3), and the Grüniesen gamma terms (B0, B1). The experimental values of A2 and A3 were set to zero as it provided the best overall response with all types of planar plate impact tests performed in [8].

Table 5 Estimated and experimentally derived equation of state properties of the UMS2526/Krempel BD laminate.

Parameter	*Theory*	*Experiment*
Bulk Modulus A1 [GPa]	28.24	25.04
Parameter A2 [GPa]	5.35	0
Parameter A3 [GPa]	16.97	0
Parameter B0 []	2.496	1.098
Parameter B1 []	2.496	1.098
Parameter T1 [GPa]	28.24	25.04
Parameter T2 [GPa]	5.35	0

Hugoniot reference curves defined by the parameters in Table 5 are shown in Figure 2b. The calculated curve shows a non-linear increase with compression, whereas the experimental curve shows a constant linear relationship.

3.2 Characterising irreversible, non-linear damage

Similarly to the orthotropic elastic properties, prediction of laminate irreversible plastic damage begins on a micromechanics level. For the prediction of strength, there exist significantly more micromechanical theories than for elasticity; however they are less accurate in general and subsequently less widely accepted. Strength characteristics of composite materials are very sensitive to pre-existing material defects, which must be considered in any strength-based model. In the derivation of material stress, integrated averages are usually expressed for the material volume, smoothing the local stress and strain perturbations. However, in mechanical testing of composite materials, failure initiation often occurs in defective regions, thus their effect is very significant. Two simple strength models are assessed for their accuracy in predicting the strength properties of the three CFRP composites used previously: the strength equations of Chamis [13] and a continuation of the bridging model [18]. In the following X, Y and S_{xy} refer to strength in the longitudinal, transverse, and in-plane shear directions respectively. The subscripts t and c indicate tensile and compressive strengths, respectively.

The average variance of the micromechanics strength predictions from the measured properties of the three CFRP composites is shown in Figure 3a. The strength of materials predictions provide better agreement with the measured properties that those of the bridging model, with the exception of longitudinal compression strength, X_c. Similar to the elastic models, the accuracy of the methods is found to depend on the material data source. In the strength of materials theory, longitudinal compression strength is calculated as the minimum of three different possible failure mechanisms: fibre compression, delamination, and microbuckling. Figure 3b shows, that by ignoring the delamination failure mechanism, agreement of the prediction with the reported composite properties considerably increases. As such, for the prediction of CFRP compression strength this failure mechanism is not considered.

Laminate strength properties are calculated, in general, by the analysis of stress and strains in each individual ply which are checked against ply failure criteria. Once failure in an individual ply has occurred, degradation models are used to re-evaluate the contribution of failed plies to the continuing load performance of the intact laminate. The World Wide Failure Exercise (WWFE) [29] assessed the maturity and capability of nineteen leading theoretical approaches for predicting the deformation and failure response of polymer composite laminates when subject to complex states of stress. Puck's action plane failure theory [30] was deemed the "winner" of the exercise, based on a systematic comparison with experimental measurements. Puck's failure theory defines two independent fracture criteria to determine lamina strength: fibre failure (FF) and inter-fibre failure (IFF) within the matrix. The FF criterion is based on a modified version of the maximum stress criteria, in which the effect of stress magnification caused by the differing constituent modulii during biaxial loading is taken into account:

$$\frac{1}{\varepsilon_{1T}}\left(\varepsilon_1 + \frac{\nu_{f12}}{E_{f11}} m_{\sigma f}\,\sigma_2\right) = 1 \text{ for } (\ldots) \geq 1 \qquad (23)$$

$$\frac{1}{\varepsilon_{1C}}\left|\left(\varepsilon_1 + \frac{\nu_{f12}}{E_{f11}} m_{\sigma f}\,\sigma_2\right)\right| + \left(10\bar{\gamma}_{21}\right)^2 = 1 \text{ for } (\ldots) < 0 \qquad (24)$$

where $m_{\sigma f}$ is the mean magnification factor of the transverse stress (fibre).

The IFF criterion is based on the Mohr failure criteria. Three IFF modes (A, B and C) were identified by Puck, and are used to generate a so-called master fracture curve, shown in Figure 4. Mode A corresponds to failure under applied transverse tension or in-plane shear; mode B corresponds to a longitudinal shear failure under high applied shear stress and moderate transverse compression stress; and mode C describes failure that occurs on an inclined fracture plane under a combination of high applied transverse compression and shear stresses. These modes are described mathematically as:

Mode A ($\sigma_2 \geq 0$): (25)

$$f_E\,|_{\sigma_{fp=0^\circ}} = \frac{1}{R_{\perp\|}}\left[\sqrt{\left(\frac{R_{\perp\|}}{R_{\perp}^{(+)}} - p_{\perp\|}^{(+)}\right)\sigma_2^2 + \tau_{21}^2} + p_{\perp\|}^{(+)}\sigma_2\right] = 1$$

Mode B ($\sigma_2 < 0$): (26)

$$f_E\,|_{\theta_{fp}=0^\circ} = \frac{1}{R_{\perp\|}}\left[\sqrt{\tau_{21}^2 + \left(p_{\perp\|}^{(-)}\sigma_2\right)^2} + p_{\perp\|}^{(-)}\sigma_2\right] = 1$$

Mode C ($\sigma_2 < 0$): (27)

$$f_E\,|_{\theta_{fp}\neq 0^\circ} = \frac{\tau_{21}^2}{4\cdot\left(R_{\perp\|} + p_{\perp\|}^{(-)}R_{\perp\perp}^{A}\right)^2}\cdot\frac{R_{\perp}^{(-)}}{(-\sigma_2)} + \frac{(-\sigma_2)}{R_{\perp}^{(-)}} = 1$$

where $R_{\perp}^{(+)}$ is the transverse tensile strength of a unidirectional laminate
$R_{\perp}^{(-)}$ is the transverse compressive strength of a unidirectional laminate
$p_{\perp\|}^{(+)}$ & $p_{\perp\|}^{(-)}$ are the fracture surface inclination parameters

Puck's theory is used to calculate the in-plane stress-strain performance of the composite laminate, using the constants given in Table 6.

Table 6 Parameter values for Puck's theory

Constant	*Symbol*	*Value*
Inclination parameter	$p_{12}^{(+)}$	0.35
Inclination parameter	$p_{12}^{(-)}$	0.3
Inclination parameter	$p_{22}^{(+/-)}$	0.3
Degradation constant	c	4
Degradation constant	ξ	2
Remaining stiffness	η_r	0.25

The onset of non-linear, irreversible damage is defined in the advanced orthotropic composite material model by a quadratic yield function [11]. To describe the limit of reversible loading, the yield function requires a master effective stress-effective plastic strain curve and nine plasticity coefficients which define the degree of anisotropy of the hardening surface. For the UMS2526/Krempel BD laminate, the laminate 22-direction is used to define the master curve (thus, the corresponding plasticity parameter $a_{22} = 1.0$). The remaining in-plane plasticity parameters are using Poisson's ratios calculated from the derived in-plane σ-ε curves:

$$a_{11} = a_{22}\frac{\nu_{21}^{p}}{\nu_{12}^{p}} \qquad a_{22} = a_{11}\frac{\nu_{12}^{p}}{\nu_{21}^{p}} \qquad a_{12} = -a_{22}\nu_{21}^{p} \tag{28}$$

The remaining in-plane and shear plasticity parameters can be defined by simplifying the elastic-plastic stress-strain performance of the laminate under the relative loading conditions to either perfectly elastic ($\overline{\sigma}_L = \overline{\sigma}_{\#1}$), or perfectly elastic-plastic ($\overline{\sigma}_L = \overline{\sigma}_{\#10}$):

$$a_{ii} = \frac{2}{3}\left(\frac{\overline{\sigma}_L}{\sigma_{ii,ULT}}\right)^2 \quad \text{in unidirectional loading (i = 1,2,3)} \tag{29}$$

$$a_{rr} = \frac{1}{3}\left(\frac{\overline{\sigma}_L}{\tau_{ij,ULT}}\right)^2 \quad \text{in shear loading (i} \neq \text{j, r = 4,5,6)} \tag{30}$$

The plasticity coefficients a_{13} and a_{23} are approximated using idealised assumptions, e.g. under loading in the 22-direction, the laminate Poisson's ratio is adopted for the plastic Poisson's ratio, effectively defining a rate of transverse plastic strain equal to the elastic transverse strain once the 1st yield condition has been fulfilled. Under loading in the through-thickness direction, minimal plastic strain is expected in the 11-direction due to the high axial stiffness of the fibres, therefore $a_{13} \cong 0$.

The calculated irreversible, non-linear damage properties of the UMS2526/Krempel BD laminate are listed in Table 7, compared to those determined experimentally in [8]. The theoretically-derived master curve shows significantly higher effective stress values than the experimentally-determined values as a result of the higher predicted directional strength. These higher effective stress values result in higher out-of-plane shear stress plasticity parameters (a_{44} and a_{55}) as well as a higher through-thickness plasticity parameter (a_{33}). The effect of these variations can be considered by visually comparing the defined failure surface. However, as the quadratic yield function is six-dimensional in stress space, it is impossible to visualise the described surface. By simplifying the yield function to consider only normal (Eq. (31)) or only shear stresses (Eq. (32)), a visualization can be made.

$$f\left(\sigma_{ij}\right) = a_{11}\sigma_{11}^2 + a_{22}\sigma_{22}^2 + a_{33}\sigma_{33}^2 + 2a_{12}\sigma_{11}\sigma_{22} + 2a_{23}\sigma_{22}\sigma_{33} + 2a_{13}\sigma_{11}\sigma_{33} = k \tag{31}$$

$$f\left(\sigma_{ij}\right) = 2a_{44}\sigma_{23}^2 + 2a_{55}\sigma_{31}^2 + 2a_{66}\sigma_{12}^2 = k \tag{32}$$

Figure 5a shows the theoretically- and experimentally-derived limit surface defining the onset of non-linear irreversible strain in normal stress space. Although both surfaces form a closed ellipse, the experimentally-derived surface is significantly more elongated than the theoretical surface. This is due to an assumption in the experimentally-characterised data set of no plastic strain in the material 11-direction, which ensures directional failure occurs prior to the onset of inelastic strain. For the theoretical data set, a small degree of plasticity was predicted.

The curves shown on the failure surfaces in Figure 5a correspond to cross section plots, an example of which is given in Figure 5b for the theoretical data set at $\sigma_{33} = 0$.

Table 7 Derived strength model properties of the UMS2526/Krempel BD laminate.

Parameter	*Theory*	*Exp.*	*Parameter*	*Theory*	*Exp.*
A11 []	0.364	0.025	Eff. Stress #1 [MPa]	404.277	120.025
A22 []	1	1	Eff. Stress #2 [MPa]	411.432	145.745
A33 []	3.576	0.660	Eff. Stress #3 [MPa]	418.587	168.157
A12 []	-0.341	-0.1285	Eff. Stress #4 [MPa]	427.416	186.774
A13 []	0	0	Eff. Stress #5 [MPa]	438.265	199.633
A23 []	-0.3345	-0.473	Eff. Stress #6 [MPa]	465.098	210.166
A44 []	23.066	3.157	Eff. Stress #7 [MPa]	491.930	218.984
A55 []	21.405	2.128	Eff. Stress #8 [MPa]	518.763	227.068
A66 []	0.388	0.061	Eff. Stress #9 [MPa]	536.651	232.702
			Eff. Stress #10 [MPa]	549.173	238.825
			Eff. Plastic Strain #1 []	0	0
			Eff. Plastic Strain #2 []	2.701E-6	1.7236E-4
			Eff. Plastic Strain #3 []	8.295E-6	3.4473E-4
			Eff. Plastic Strain #4 []	1.697E-5	5.1709E-4
			Eff. Plastic Strain #5 []	3.997E-5	6.8945E-4
			Eff. Plastic Strain #6 []	1.670E-4	8.6140E-4
			Eff. Plastic Strain #7 []	3.676E-4	0.00103
			Eff. Plastic Strain #8 []	6.907E-4	0.00121
			Eff. Plastic Strain #9 []	9.088E-4	0.00138
			Eff. Plastic Strain #10 []	1.070E-3	0.00155

3.3 Characterising failure initiation

In [8] uniaxial quasi-static tensile tests were used to determine laminate in-plane strength properties. However, for the through-thickness tensile strength, dynamic spall flyer plate impact tests were performed in which the loading rate (impact velocity) varied from 159 m/s to 1073 m/s and an average value, based on the three best spallation signals, was defined (shown in Figure 6).

This average dynamic tensile strength is significantly higher than what would be expected for a quasi-static though thickness tensile test. It is considered that the through-thickness tensile strength is limited by the allowable tensile strain in the matrix, which varies dependent on loading rate (see e.g. [31]), resulting in the varying spallation strengths measured in [8]. Unless dynamic loading conditions equivalent to those induced during hypervelocity impact can be generated, the definition of dynamic tensile strength in the through-thickness direction is somewhat arbitrary. For the theoretical derivation, the through-thickness tensile strength is estimated as a quasi-static property, based on the methodology for calculating the transverse tensile strength of a unidirectional laminate in [32]. A maximum tensile strain of 2% is adopted for the Krempel BD epoxy resin.

$$\sigma_{33} = \varepsilon_{\max}^{m} \cdot E_{33} \tag{33}$$

In [13] micromechanics equations for calculating the longitudinal and transverse interlaminar shear strengths of unidirectional laminates are presented:

Longitudinal:

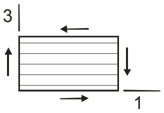

$$S_{13} = \left[1 - \left(\sqrt{V_f} - V_f\right)\left(1 - \frac{G_m}{G_{f12}}\right)\right] S_m \tag{34}$$

Transverse:

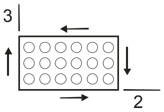

$$S_{23} = \left[\frac{1 - \sqrt{V_f}\left(1 - G_m / G_{f23}\right)}{1 - V_f\left(1 - G_m / G_{f23}\right)}\right] S_m \tag{35}$$

A simple scaling between the two limits is made, where a scaling parameter (χ) is defined based on the alignment of the individual layers in the composite laminate. The transverse shear strengths (S_{23}, S_{31}) are then estimated using:

$$S_{ij} = S_{long}\chi_{ij} + S_{trans}\left(1 - \chi_{ij}\right) \tag{36}$$

where $\chi_{ij} = \sum_{k=1}^{no.plies} \cos\varphi_k \frac{t_k}{t}$ and

φ_k – Angle of ply relative to load plane
t_k – Thickness of ply k
t – Thickness of laminate

The failure properties calculated for the UMS2526/Krempel BD laminate are given in Table 8, compared to the experimentally-measured values. Significant variation is noted for many of the failure properties, particularly the tensile failure stress in the 22-direction. To a degree this is to be expected as (noted previously) the theoretical calculation of composite strength properties is subject to large variation due to the dependence of composite material strength on the presence of manufacturing defects. As such, although the applied theories have been selected based on their accuracy for similar materials, a significant degree of variation from experimentally-measured values is to be expected. With the exception of σ_{22} (223%), and τ_{23} (169%), all strength predictions are within ± 50% of the experimental values. In the case of hypervelocity impact, in which impact pressures exceed material strengths by orders of magnitude, this is not expected to have a significant effect on the overall result of an impact simulation (i.e. structural perforation). However, the lateral extension of damage is expected to be adversely effected.

Table 8 Theoretically and experimentally derived failure properties of the UMS2526/Krempel BD laminate.

Parameter	*Theory*	*Experimental*
Tens. Failure Stress 11 [MPa]	901.177	619
Tens. Failure Stress 22 [MPa]	448.398	195
Tens. Failure Stress 33 [MPa]	174.20	245.7
Max. Shear Stress 12 [MPa]	374.639	280.5
Max. Shear Stress 23 [MPa]	66.018	39.0
Max. Shear Stress 31 [MPa]	68.524	47.5

3.4 Characterising non-linear softening

CFRP laminates usually fail in a brittle-type fracture mode, regardless of load direction, thus post failure “softening” is not applicable. However, in a macromechanic model the post-fracture softening must also incorporate the effects of geometric fracture. Under in-plane tensile loading CFRP laminates exhibit brittle failure, thus:

$$G_{f11} = G_{f22} = 0 \ \ J/m^2 \tag{37}$$

Tensile loading in the through-thickness direction is a matrix-dominated failure mode. Experimentally, this fracture energy is determined in a double-cantilever beam (DCB) test. It has been shown in [8] that under this loading type, even for highly brittle epoxy resins, fracture is not instantaneous and therefore $G_{f33} \neq 0$. For mode-I delamination of the laminate, the fracture energy of the epoxy resin is adopted, thus:

$$G_{f33,ii} = G_{mf,ii} \tag{38}$$

Under in-plane shear loading, the fracture of a multi-directional CFRP composite is similarly brittle to that observed under uni-axial tensile loading. In Figure 7 the results of uni-axial tensile tests performed on a bias [±45°] CFRP laminate to simulate an in-plane shear load are shown. It is seen that upon reaching the laminate failure stress, the load-carrying capability of the laminate diminishes immediately to zero. Thus, it is reasonable to assume:

$$G_{f12} = 0 \ \ J/m^2 \tag{39}$$

For transverse shear failure (mode II) a large databank of delamination fracture toughness values for laminates was compiled in [33]. The ratio of mode II to mode I fracture toughness for polymer composites is shown in Figure 8. Although there is a large degree of scatter in the polynomial fit, it is considered to be a reasonable approximation for the transverse (i.e. loading in the through-thickness direction) mode II fracture toughness. The polynomial fit is defined as:

$$\frac{G_{IIc}}{G_{Ic}} = A' \cdot G_{Ic}{}^{-\alpha} \tag{40}$$

where A' = 59.244
α = 0.4811

The calculated post-failure, non-linear softening properties of the UMS2526/Krempel BD laminate are shown in Table 8, compared to those determined experimentally in [8]. Generally, a good degree of agreement is found. The experimentally-derived data set shows an increased fracture energy for out-of-plane shearing 23 than 31 (derived from ENF tests), probably as a result of the decreased fibre alignment in the 22-direction. The theoretical assumption, based on a relationship between mode I and mode II fracture energies of CFRP composites is unable to reproduce this difference.

Table 9 Theoretically and experimentally derived non-linear softening properties of the UMS2526/Krempel BD laminate.

Parameter	*Theory*	*Exp.*
Fracture Energy 11 [J/m^2]	1E-6	1E-6
Fracture Energy 22 [J/m^2]	1E-6	1E-6
Fracture Energy 33 [J/m^2]	240	333.5
Fracture Energy 12 [J/m^2]	1E-6	1E-6
Fracture Energy 23 [J/m^2]	1018	1378
Fracture Energy 31 [J/m^2]	1018	747

4 Application of the Material Model for Simulation of Space Debris Impact

Two hypervelocity impact experiments have been performed on EMI's two-stage light-gas guns to assess the effect of material data on the accuracy of numerical simulation damage predictions and the applicability of the theoretical derivation procedure.

4.1 Target set-up

Two experimental set-ups using the UMS2526/Krempel BD laminate were considered: (1) a CFRP/Al honeycomb sandwich panel with 1.37 mm thick CFRP facesheets and a 25mm thick Al honeycomb core, and (2) two 1.37 mm thick CFRP laminates with 25mm spacing between them. Target 1 was subject to oblique (60°) impact of a 1.775 mm Al-sphere at 6.095 km/s (EMI no. 4848), and target 2 was subject to normal impact (perpendicular to the target surface) of a 1.179 mm Al-sphere at 4.935 km/s (EMI no. 236). The two target configurations are shown in Figure 9.

In Figure 10 a comparison between the experimentally-induced (both visual and ultrasonic) and numerically-predicted damage in on Target 1 (EMI no. 4848) is shown. On the experimental target a roughly circular perforation is observable on the front facesheet, with a number of small cracks are barely visible on the rear facesheet. The ultrasonic scan reveals more significant internal damage (delamination). The honeycomb core shows a damage cone biased to one side due to the oblique impact velocity vector (to right of page). The numerical simulation applying the experimentally-characterised data set from [8] shows a near-triangular shaped perforation hole in the front facesheet and two separate areas of damage are observable on the rear facesheet: one large perforation hole corresponding to debris ejected normally from the front facesheet, and a second smaller perforation biased in the direction of the impact velocity vector. The damage to the honeycomb core is significantly less than that observed in the experiment. The numerical simulation applying the data set derived from the theoretical procedure also shows a non-circular perforation hole in the front facesheet (although dimensions of the perforation hole are comparable with the experiment) and two separate perforation holes in the rear facesheet. The perforation hole dimensions and locations are similar to those in the experimentally-characterised numerical simulation.

In general, a comparison of the predicted damage in the two numerical models shows little difference. The experimentally-characterised data set predicts larger delamination in the front CFRP facesheet, agreeing more closely to the damage seen in the ultrasound image. Conversely, the honeycomb core shows considerably more damage in the theoretically-characterised model than the experimentally-characterised numerical model, however it is still much less than that observed in the experiment. The reduced extension of damage in the numerical model honeycomb cores suggests the Al-foils of the honeycomb may have been modelled overly strong, restricting expansion of the fragment cloud and channelling the debris to a more localised area on the rear facesheet (which could justify the increased rear facesheet penetration damage prediction in the numerical model).

For the second impact test (EMI no. 236), damage induced by the normal impact of a 1.179 mm Al-sphere at 4.935 km/s target 2 is shown in Figure 11 compared to the simulated damages using both the experimentally-and numerically-characterised data sets. The experimental result shows a clear perforation hole in the front facesheet and a small amount of cracking on the rear facesheet. Ultrasonic scans of the rear facesheet show internal damage (delamination). Both numerical models show similar predictions, predicting a circular perforation hole in the front facesheet and no noticeable damage on the back of the rear facesheet. As with simulation of the oblique impact experiment, the numerical simulation using the experimentally-characterised data set shows significantly more delamination in the front facesheet than the theoretically-characterised model. This represents the major difference between the two models in predicting the damage induced by impact of a space debris particle at hypervelocity.

In Table 10 the damage measurements made from the experiment and numerical simulations are presented. As shown in Figure 10 and Figure 11, the agreement between the experimental damages and numerical predictions are quantitatively acceptable with the exception of predicted perforation of the sandwich panel rear facesheet in EMI experiment 4848 which is considered to be a result of excessively channelling of projectile fragments by the overly-strong honeycomb core cell walls.

Table 10 Comparison of experimental and numerical (both experimentall-0characterized and theoretically-characterized material data sets) damage measurements.

	Front facesheet				*Rear facesheet*				*HC*
Target	$d_{h,1}$ *(cm)*	$d_{h,2}$ *(cm)*	$D_{h,1}$ *(cm)*	$D_{h,1}$ *(cm)*	$d_{h,1}$ *(cm)*	$d_{h,1}$ *(cm)*	$D_{h,1}$ *(cm)*	$D_{h,1}$ *(cm)*	d_{HC} *(cm)*
4848									
Experiment	5.3	7.0	40	15	-	-	53	33	22
Sim (exp.)	7.2	6.0	35	19	6.3	7.0	13	14	11
Sim (theor.)	7.9	8.4	23	25	6.0	5.1	14	13	13
236									
Experiment	3.0	3.1	39	14	-	-	29	13	N/A
Sim (exp.)	2.6	3.1	19	18	-	-	14	18	N/A
Sim (theor.)	3.3	3.3	28	16	-	-	22	14	N/A

5 Summary and Conclusions

A procedure has been defined that allows derivation of a composite laminate data set for application with the advanced orthotropic composite material model implemented in the commercial hydrocode ANSYS® AUTODYN®. The derivation procedure requires constituent material properties and applies micromechanics, classical laminate theory, Hooke’s law for orthotropic composites, Puck’s action plane failure criteria, and Chen’s quadratic yield function to describe the mechanical performance of a composite laminate under hypervelocity impact. The material EOS is defined as a polynomial formulation of the Mie-Grüneisen EOS, which uses an effective bulk modulus calculated from the stiffness matrix and polynomial terms derived from a general EOS defined for CFRP laminates. The post-failure performance of the laminate is described in terms of a damage algorithm that requires directional fracture energies determined from approximated properties and a mode I:mode II fracture energy relationship. A carbon fibre/epoxy composite laminate representative of those used in spacecraft primary structures has been used for verification of the derivation procedure. Towards this end a comparison between theoretically- and experimentally-characterised properties has been made. The laminate elastic properties have been satisfactorily predicted to within ± 30% of the experimentally-measured values, however the strength parameters (particularly in the material 22-direction) were, in general, over-predicted. For the equation of state, differing assumptions by the authors from those used in definition of the experimental data set (from [8]) led to differences in the polynomial terms and the degree of anisotropy in the hardening surface. Numerical simulations of hypervelocity experiments on spaced CFRP dual-wall targets and honeycomb sandwich panels with CFRP facesheets were performed with the experimentally- and theoretically-characterised material data sets. In a comparison with experimental measurements, it was found that both numerical models were qualitatively able to reproduce impact processes and damages. For normal impact on a spaced dual-wall configuration slight cracking and internal delamination of the rear wall was observed in the experiment. Both numerical models showed no damage on the back face of the rear wall. For oblique impact on a CFRP/Al honeycomb sandwich panel small cracks and internal delamination were observed on the rear CFRP facesheet in the experiment. Both numerical models predicted a clear perforation result, however this over-prediction of damage may be the effect of overly-capable honeycomb core foils, which act to channel the fragment cloud. Quantitatively, the numerical simulations using the theoretically-characterized material data set were able to reproduce front facesheet damage measurements to within ± 50% of the experimental results. Rear facesheet damage extension was generally underpredicted, while penetration was conservateively predicted (however, this is influenced by the honeycomb core model). The numerical model incorporating the experimentally-characterized data set showed a slight improvement in front facesheet damage prediction (agreement to within ±30%) while rear facesheet predictions provided comparable accuracy with the theoretically-characterized material data set. This suggests that for this particular case the theoretical characterisation procedure provided a very reasonable material data set suitable for application in hypervelocity impact simulations used for damage assessment.

6 References

[1] Klinkrad H. Space Debris – Models and Risk Analysis, Springer-Verlag, Berlin, 2006.

[2] Inter-Agency Space Debris Coordination Committee. IADC Space Debris Mitigation Guidelines, www.iadc-online.org, 2002.

[3] Liou J, Johnson N. Instability of the Present LEO Satellite Populations, Advances in Space Research 2007; DOI: 10.1016/j.asr.2007.04.081

[4] Hayhurst C, Livingstone I, Clegg R, Destefanis R, Faraud M. Ballistic Limit Evaluation of Advanced Shielding Using Numerical Simulations, Int. J. of Imp. Eng. 2001; 26; 309-320.

[5] Ryan S, Schäfer F, Spencer G, Hiermaier S, Guyot M, Lambert M. An Excitation Function for Hypervelocity Impact-Induced Wave Propagation in Satellite Structures, 57th IAC, Valencia, Oct. 2-6, 2006.

[6] Clegg R, White D, Riedel W, Harwick W. Hypervelocity impact damage prediction in composites Part I – Material model and characterisation. Int. Journal of Impact Engineering 2006; 33(1-2): 190-200.

[7] Riedel W, Nahme H, White D, Clegg R. Hypervelocity impact damage in composites Part II – Experimental investigation and simulations. Int. Journal of Impact Engineering 2006; 33(1-2): 670-680.

[8] Wicklein M, Ryan S, White D, Clegg R. Hypervelocity Impact on CFRP: Testing, Material Modelling, and Numerical Simulation, Int. J. of Imp. Eng. 2007; Accepted for publication.

[9] Lambert M, Frey J, Rios J, Garaud X, Dubois J, Schneider E. The Validation of Hydrocodes for Orbital Debris Impact Simulation, International Conference on Spacecraft Structures and Mechanical Testing, Noordwijk, April 24-26, 1991.

[10] Anderson C, Cox P, Johnson G, Maudlin P. A Constitutive Formulation for Anisotropic Materials Suitable for Wave Propagation Computer Programs – II. Computational Mechanics 1994; 15: 201-223.

[11] Chen J, Allahdadi F, Sun C. A Quadratic Yield Function for Fiber-Reinforced Composites. J. of Composite Materials 1997; 31(8): 788-811.

[12] Hou J, Petrinic N, Ruiz C. Prediction of impact damage in composite plates, Comp. Science and Technology 2000; 60:273–281.

[13] Chamis C. Simplified Composite Micromechanics Equations for Strength, Fracture Toughness and Environmental Effects, SAMPE Quarterly 1984; 15: 41-55.

[14] Halpin J. Effects of Environmental Factors on Composite Materials, Wright-Patterson AF Base, Dayton, AFML-TR-67-123, 1969.

[15] Hermans J. The Elastic Properties of Fibre Reinforced Materials When the Fibres are Aligned, K. Nederlandse Ackademie van Wetenschappen Amsterdam 1967; B70(1): 1-9.

[16] Eshelby J. The Determination of the Elastic Field of an Ellipsoidal Inclusion, and Related Problems, Proceedings of the Royal Society of London, Series A 1957; 241: 376-396.

[17] Aboudi J. Mechanics of Composite materials. A Unified Micromechanical Approach, Studies in Applied Mechanics, vol. 29, Elsevier, New York, 1991.

[18] Huang Z. A Bridging Model Prediction of the Ultimate Strength of Composite Laminates Subjected to Biaxial Loads, Comp. Science and Technology 2004; 64: 395-448.

[19] Anon. Properties for Graphite/Epoxy (IM-6/3501-6), Fiber Volume = 63.5%, University of California (San Diego), http://casl.ucsd.edu/oldindex.html, 2004.

[20] Soden P, Hinton M, Kaddour A. Lamina properties, lay-up configurations and loading conditions for a range of fibre-reinforced composite laminates. CS&T 1998; 58: 1011-22.

[21] Daniel I, Ishai O. Engineering Mechanics of Composite Materials, Oxford University Press, New York, 1994.

[22] Hart-Smith L. The Ten-Percent Rule for Preliminary Sizing of Fibrous Composite Structures, Weight Eng. 1992; 5(2): 29-45.

[23] Hiermaier S, Riedel W, Hayhurst C, Clegg R, Wentzel C. Advanced Material Model for Hypervelocity Impact Simulations, EMI, ESA CR(P) 4305, Freiburg, 1999.

[24] Riedel W, Harwick W, White D, Clegg R. Advanced Material Damage Models for Numerical Simulation, EMI, ESA CR(P) 4397, Freiburg, 2003.

[25] Riedel W, Nahme H. Shock Properties of a HEXCEL IM7/8552 – Experimental Investigations and Material Modelling, EMI, Freiburg, EMI Report E-25/01, 2001.

[26] Machens M, Schäfer F, Riedel W, Rohr I. Shock Properties of a Carbon Fibre Composite for Space Applications, EMI, Report I-36/04, Freiburg, Germany, 2005.

[27] Kawai N, Inoue K, Misawa S, Riedel W, Tanaka K, Hayashi S, Kondo K. The Dynamic Behaviour of Mortar Under Impact-Loading, Shock Compression of Condensed Matter 2007.

[28] Dugdale J, MacDonald. The Thermal Expansion of Solids, Physical Review 1953; 89(4): 832-834.

[29] Hinton M, Kaddour A, Soden P. Failure criteria in fibre reinforced polymer composites: The World Wide Failure Exercise, Elsevier, Amsterdam, 2004.

[30] Puck A, Schürmann H, Failure Analysis of FRP Laminates by Means of Physically Based Phenomenological Models. Comp. Sci & Tech. 1998; 58: 1045-1068.

[31] Gilat A, Goldberg R, Roberts G. Strain Rate Sensitivity of Epoxy Resin in Tensile and Shear Loading, Ohio State University, Columbus, NASA TM-2005-213595.

[32] Chamis C. Micromechanics Strength Theories, in: Composite Materials vol. 5 – Fracture and Fatigue, Broutman L (Edt.), Academic Press, New York, 1974.

[33] O'Brien T. Composite Interlaminar Shear Fracture Toughness, G_{IIc}: Shear Measurement of Sheer Myth?, NASA Langley Research Center, Hampton, TM-110280, 1997.

Figure 1

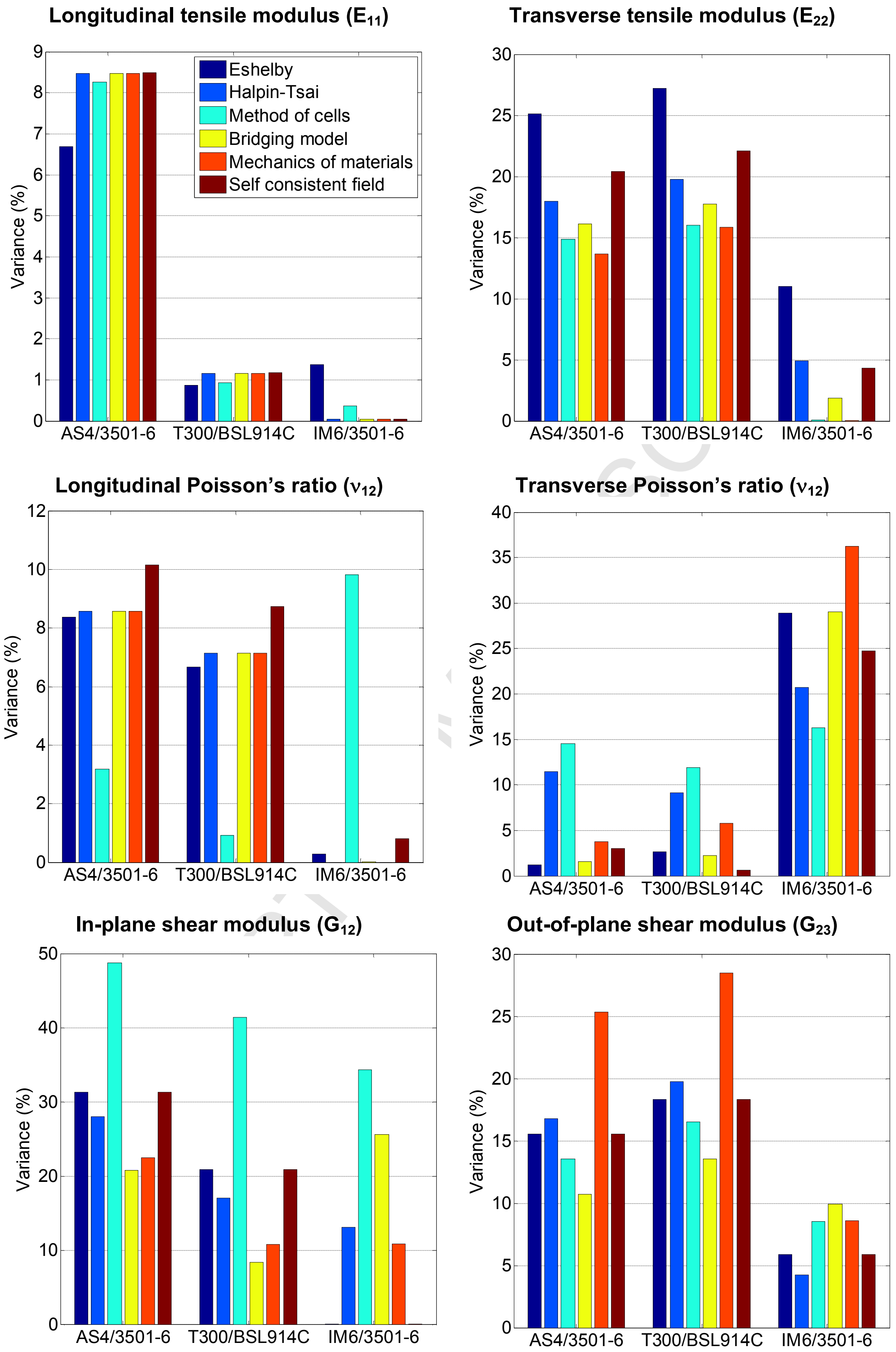

Figure 1 Accuracy of various micromechanics methods for predicting the elastic properties of AS4/3501-6 (V_f = 60%), T300/BSL914C (V_f = 60%), and IM6/3501-6 (V_f = 63.5%). Legend shown in E_{11} plot, in all cases predictions presented in order of (from left to right): Eshelby, Halpin-Tsai, Method of Cells, Bridging Model, Mechanics of Materials, Self-Consistent Field.

Figure 2a

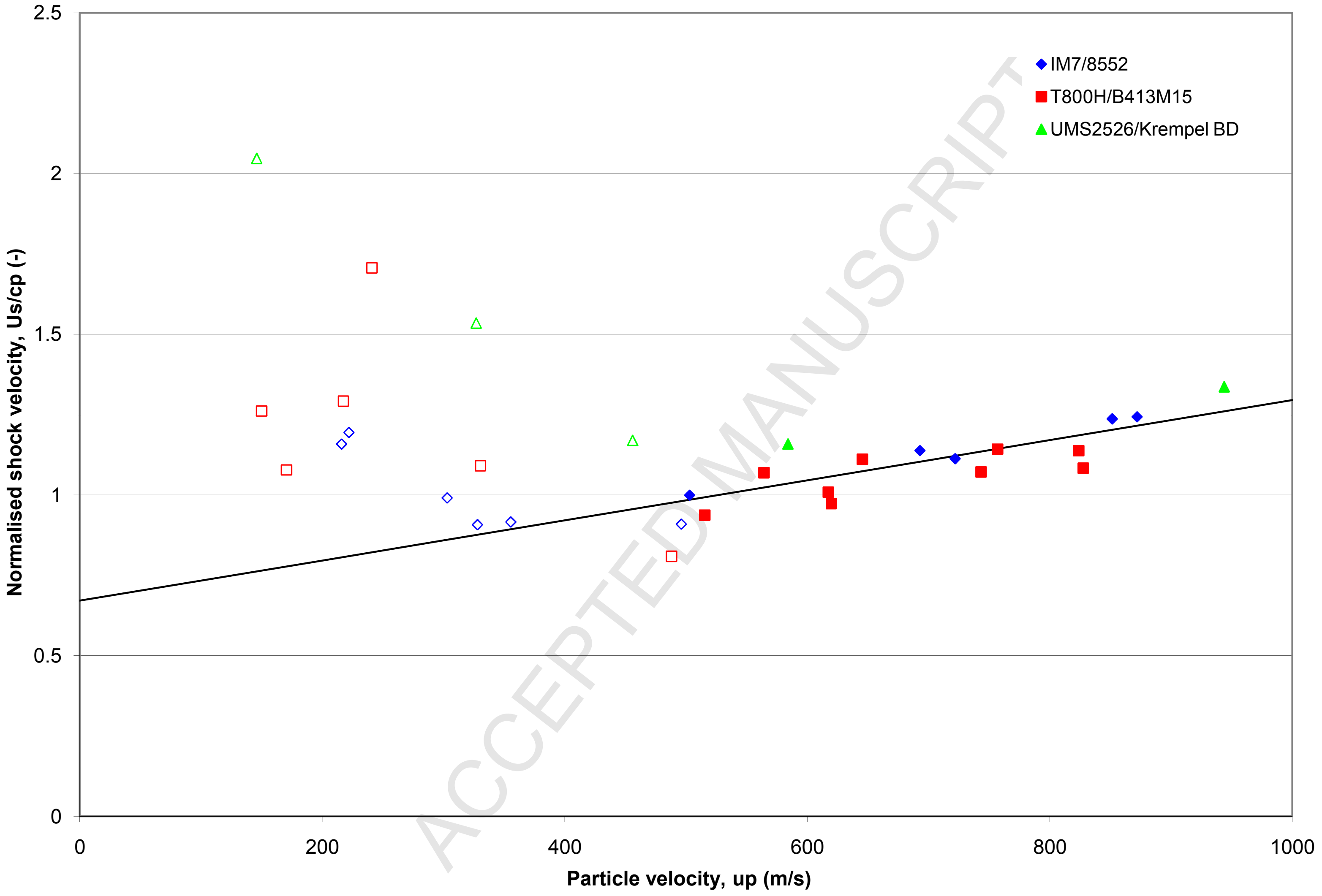
◆ IM7/8552
■ T800H/B413M15
▲ UMS2526/Krempel BD
Normalised shock velocity, Us/cp (-)
Particle velocity, up (m/s)
0
0.5
1
1.5
2
2.5
0
200
400
600
800
1000

Figure 2b

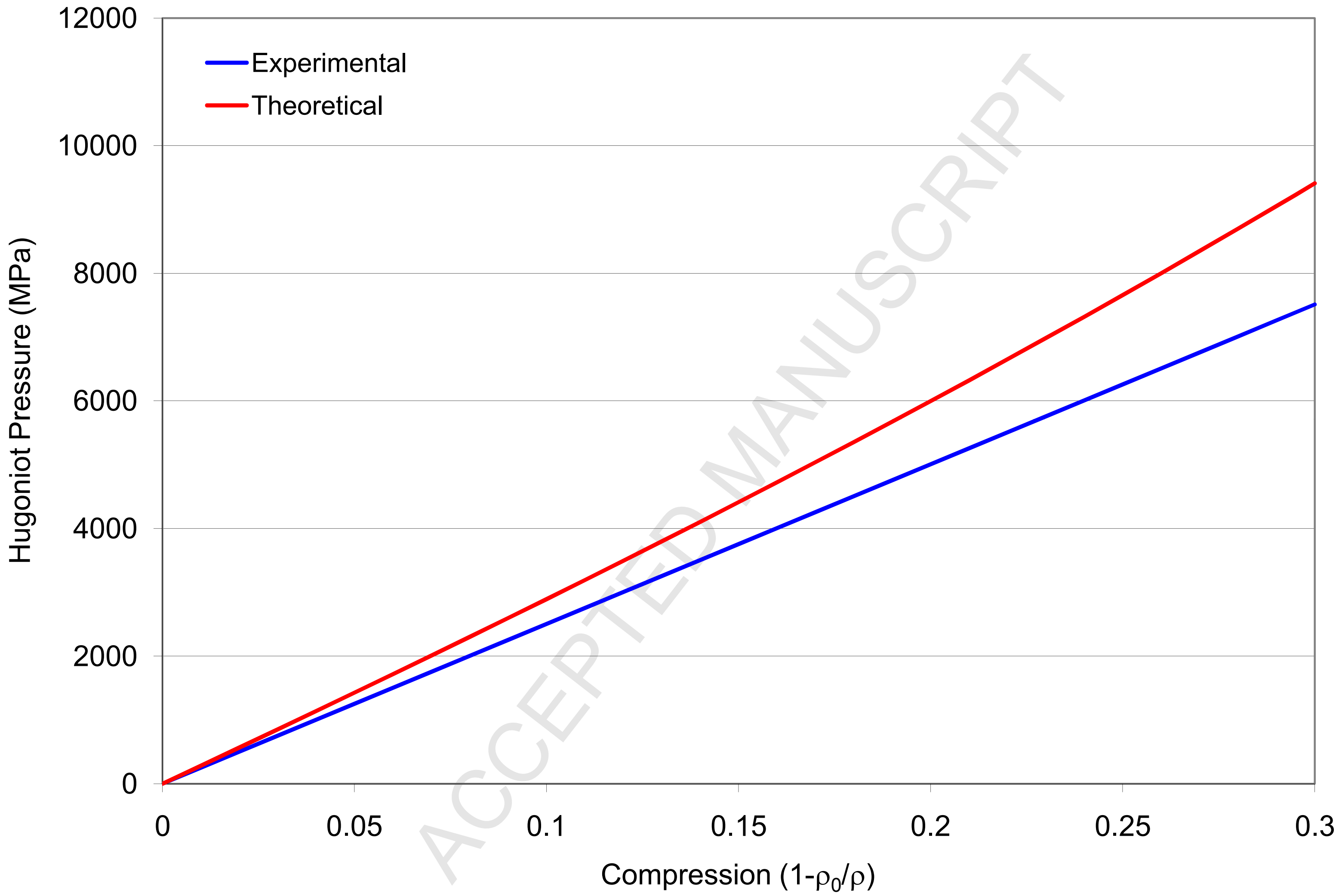
12000
10000
8000
6000
4000
2000
0
Hugoniot Pressure (MPa)
Experimental
Theoretical
0
0.05
0.1
0.15
0.2
0.25
0.3
Compression (1-ρ_0/ρ)

Figure 3a

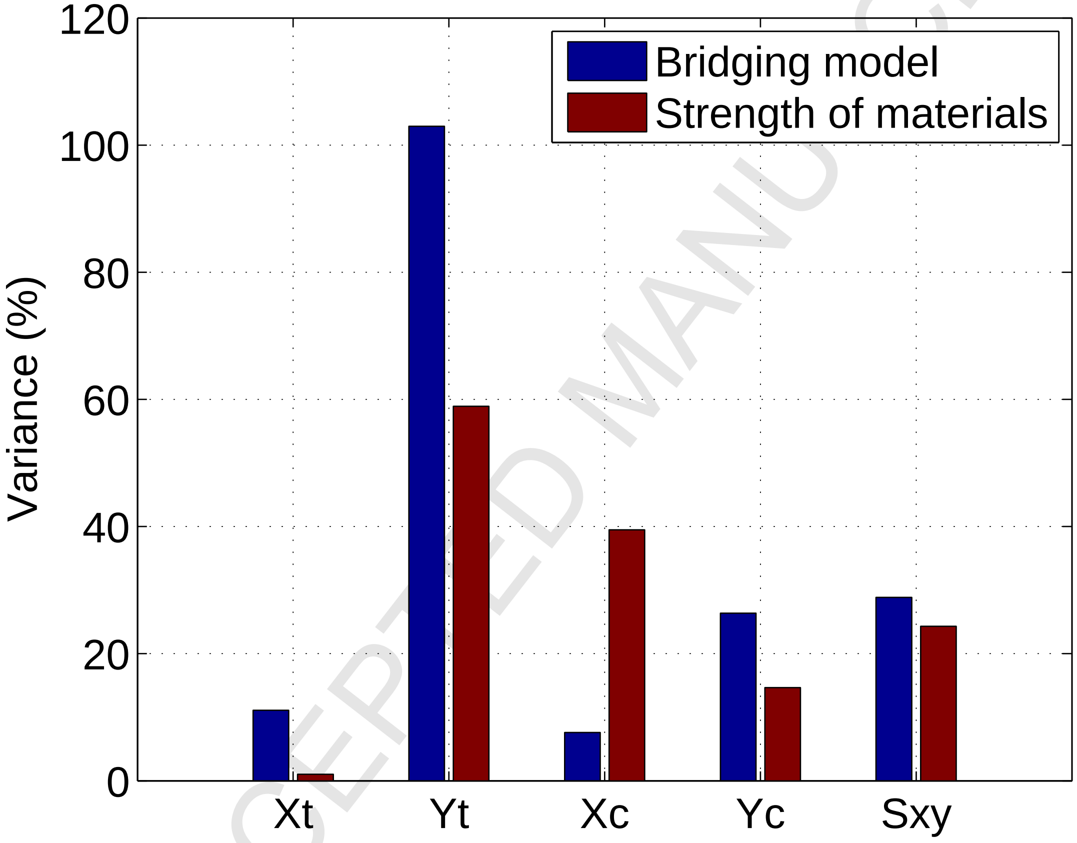
120
100
80
60
40
20
0
Variance (%)
Xt
Yt
Xc
Yc
Sxy
🟦 Bridging model
🟥 Strength of materials

Figure 3b

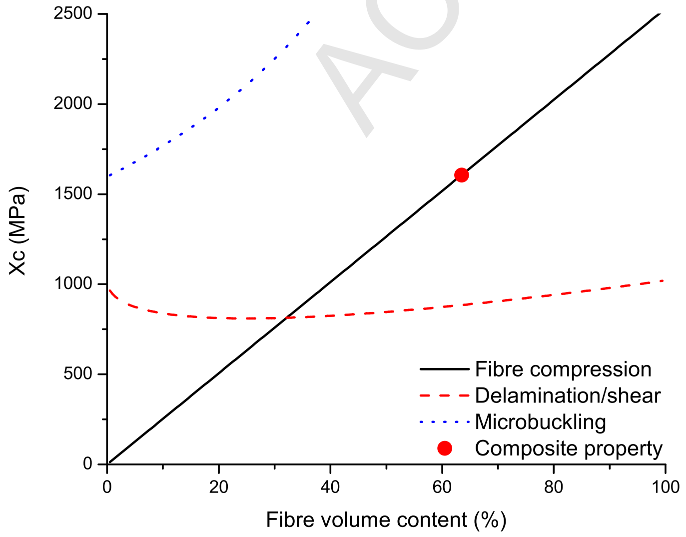
2500
2000
1500
1000
500
0
Xc (MPa)
0
20
40
60
80
100
Fibre volume content (%)
Fibre compression
Delamination/shear
Microbuckling
Composite property

Figure 4

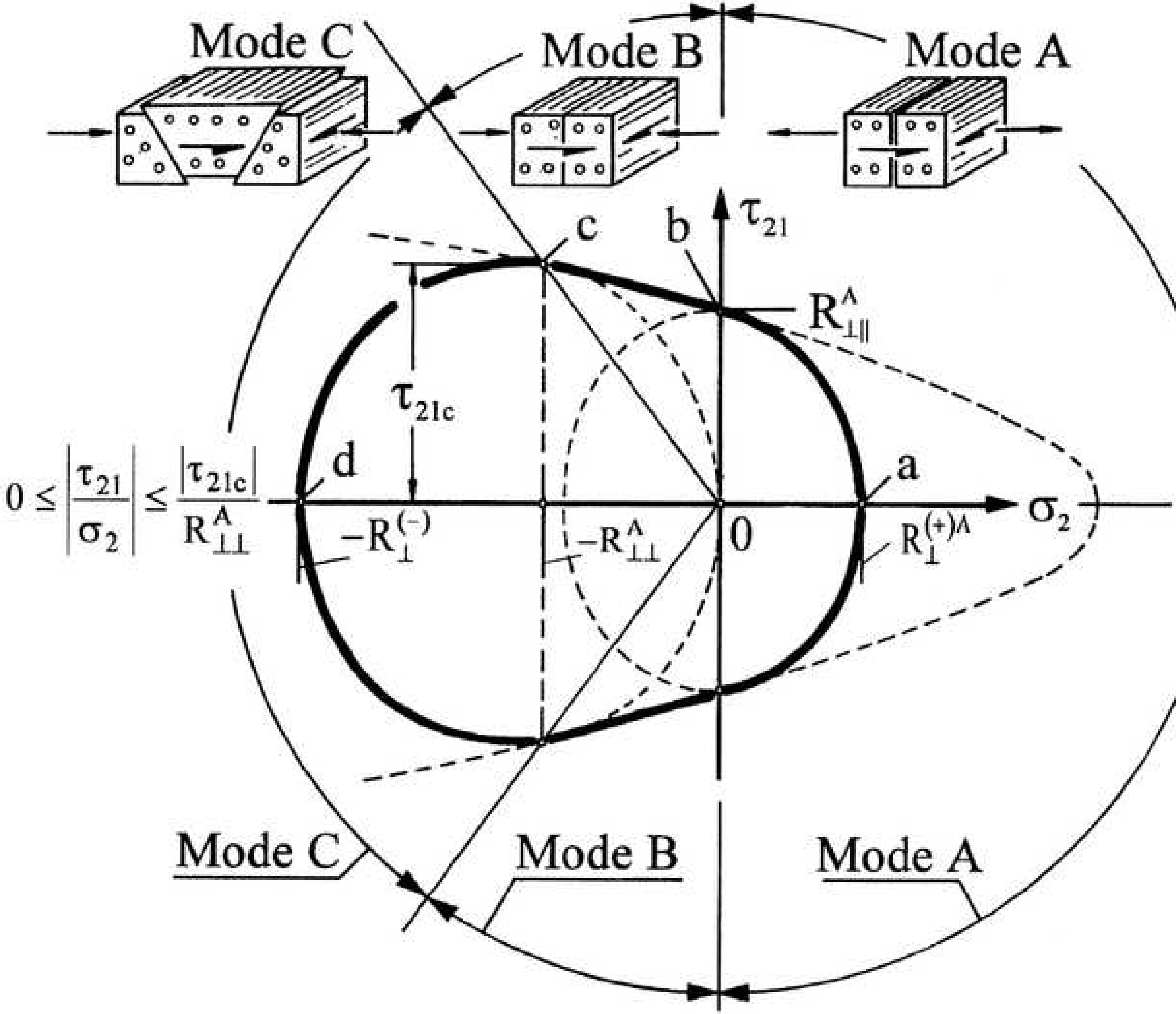
Mode C
Mode B
Mode A
τ_{21}
c
b
$R^{\wedge}_{\perp\parallel}$
τ_{21c}
d
a
σ_2
$0 \leq \left|\frac{\tau_{21}}{\sigma_2}\right| \leq \frac{|\tau_{21c}|}{R^{\wedge}_{\perp\perp}}$
$-R^{(-)}_{\perp}$
$-R^{\wedge}_{\perp\perp}$
0
$R^{(+)\wedge}_{\perp}$
Mode C
Mode B
Mode A

Figure 5a-1

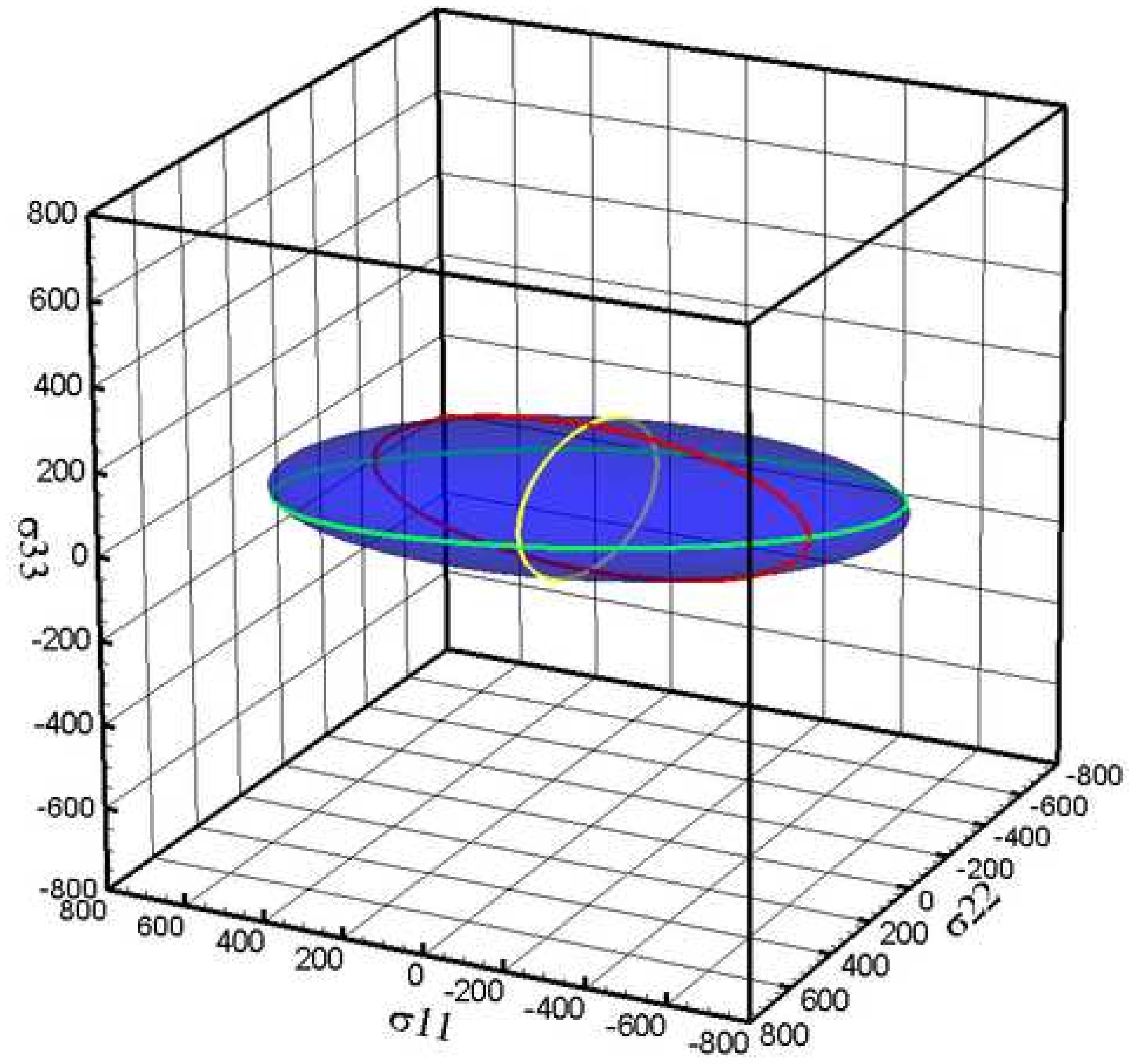
800
600
400
200
0
-200
-400
-600
-800
σ33
800
600
400
200
0
-200
-400
-600
-800
σ11
-800
-600
-400
-200
0
200
400
600
800
σ22

Figure 5a-2

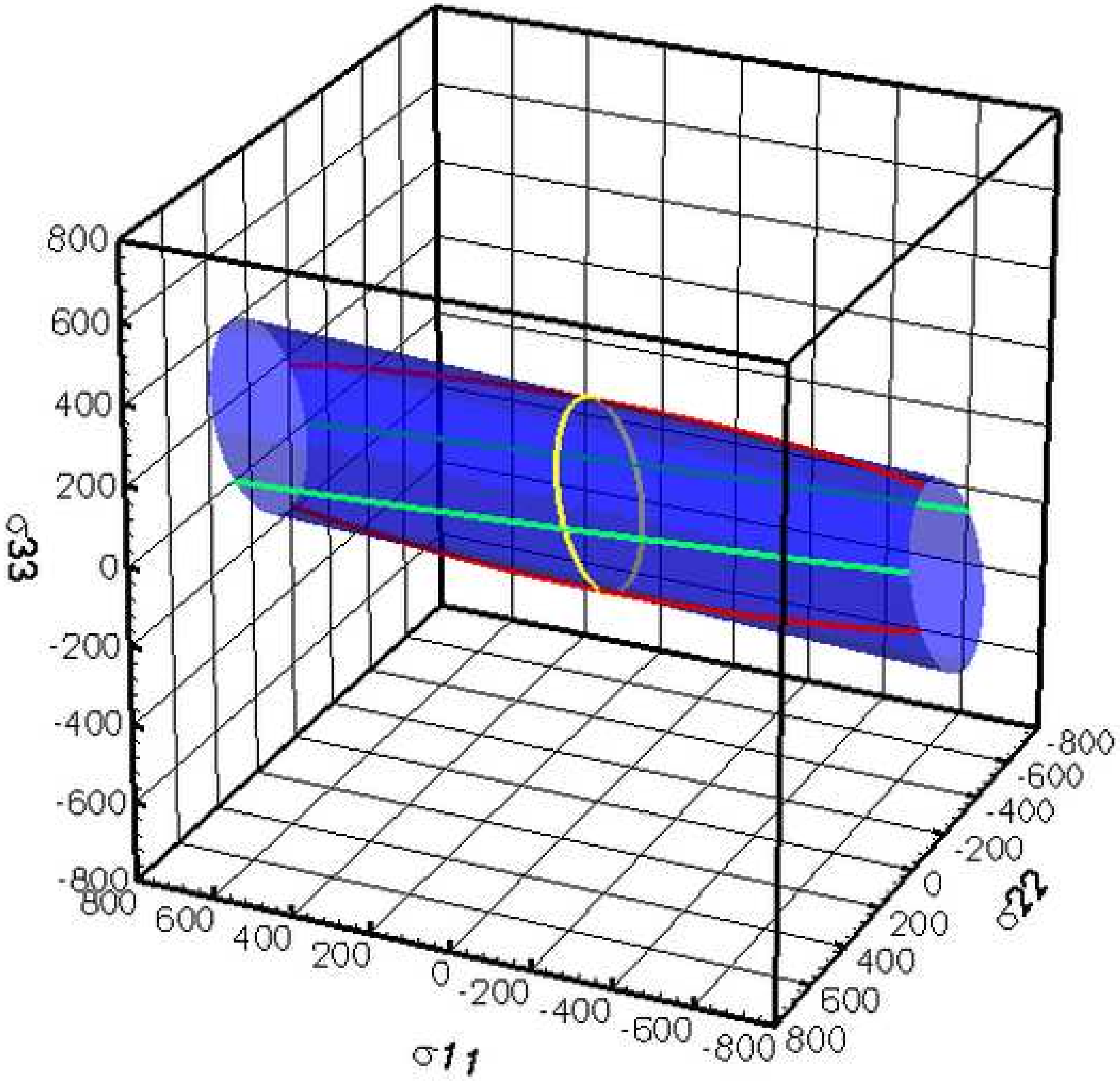
800
600
400
200
0
-200
-400
-600
-800
σ33
800
600
400
200
0
-200
-400
-600
-800
σ11
-800
-600
-400
-200
0
200
400
600
800
σ22

Figure 5b

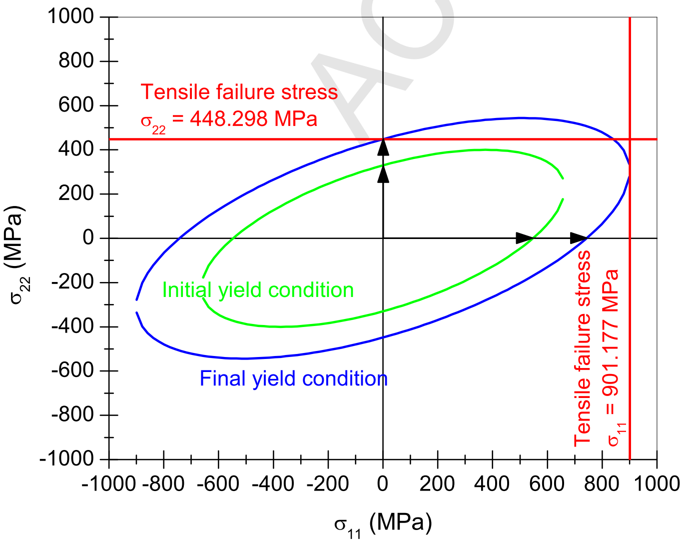
Tensile failure stress
σ_{22} = 448.298 MPa
Tensile failure stress
σ_{11} = 901.177 MPa
Initial yield condition
Final yield condition
σ_{22} (MPa)
σ_{11} (MPa)
1000
800
600
400
200
0
-200
-400
-600
-800
-1000
-1000 -800 -600 -400 -200 0 200 400 600 800 1000

Figure 6

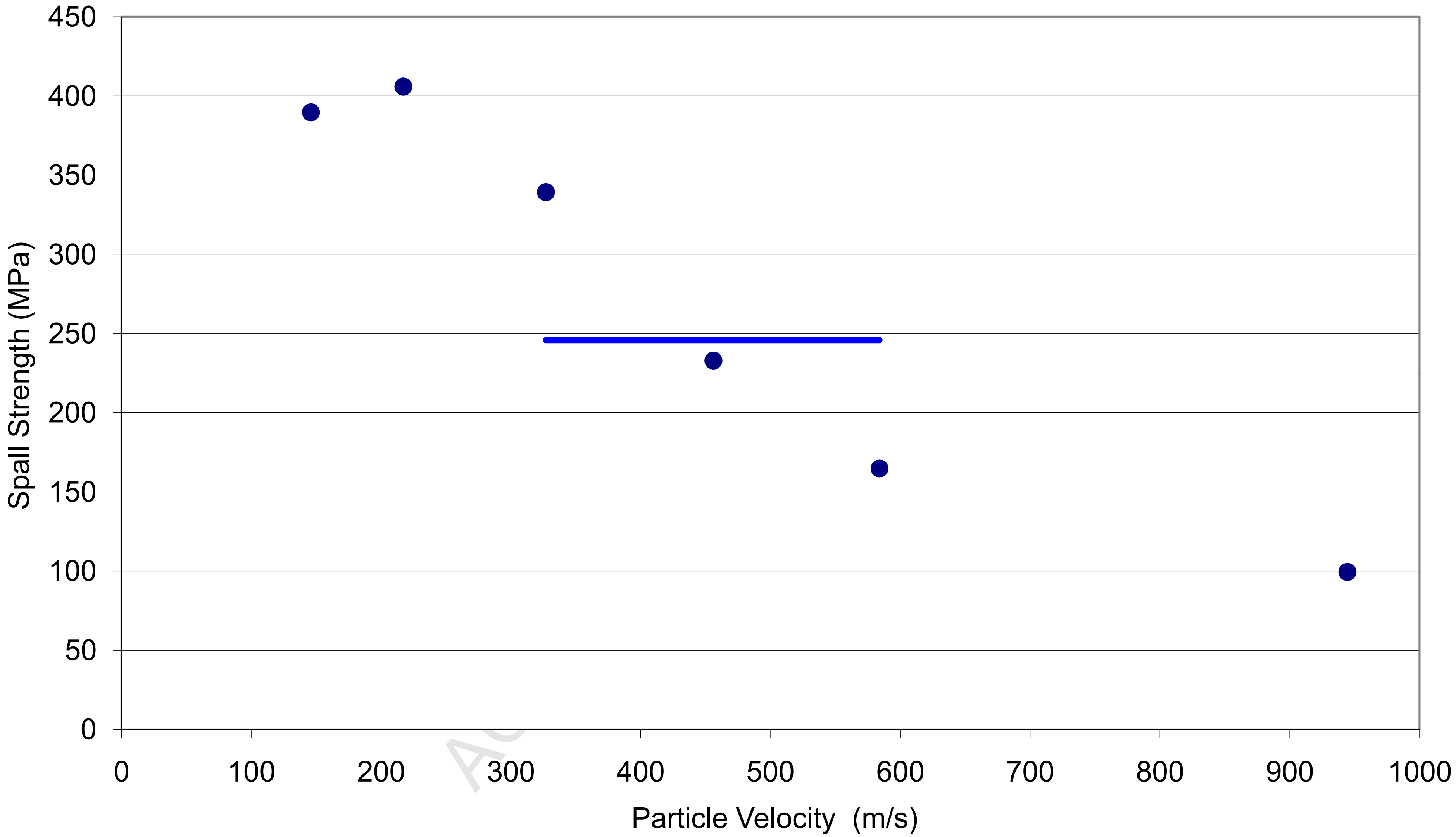
Spall Strength (MPa)
450
400
350
300
250
200
150
100
50
0
0
100
200
300
400
500
600
700
800
900
1000
Particle Velocity (m/s)

Figure 7

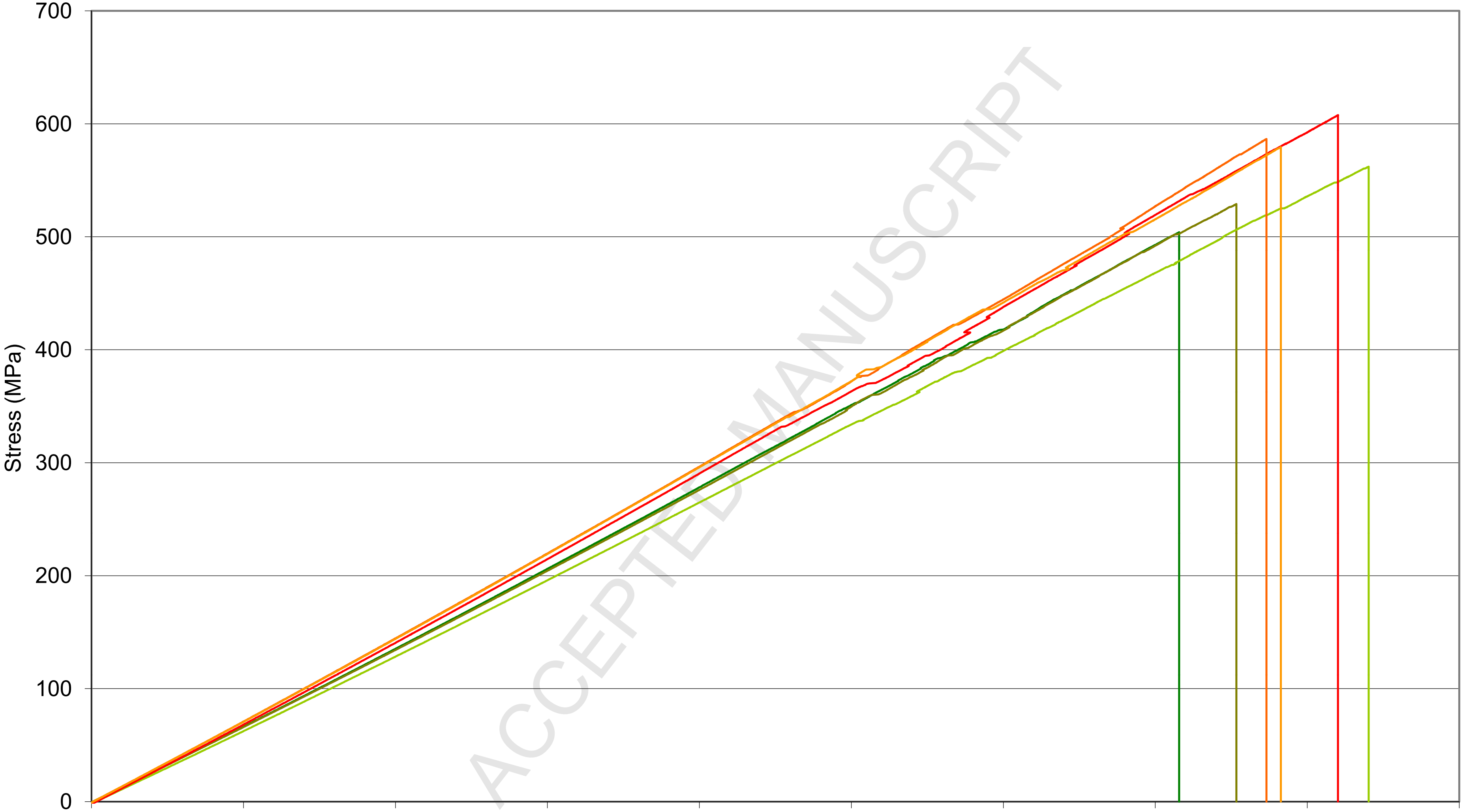

Figure 8

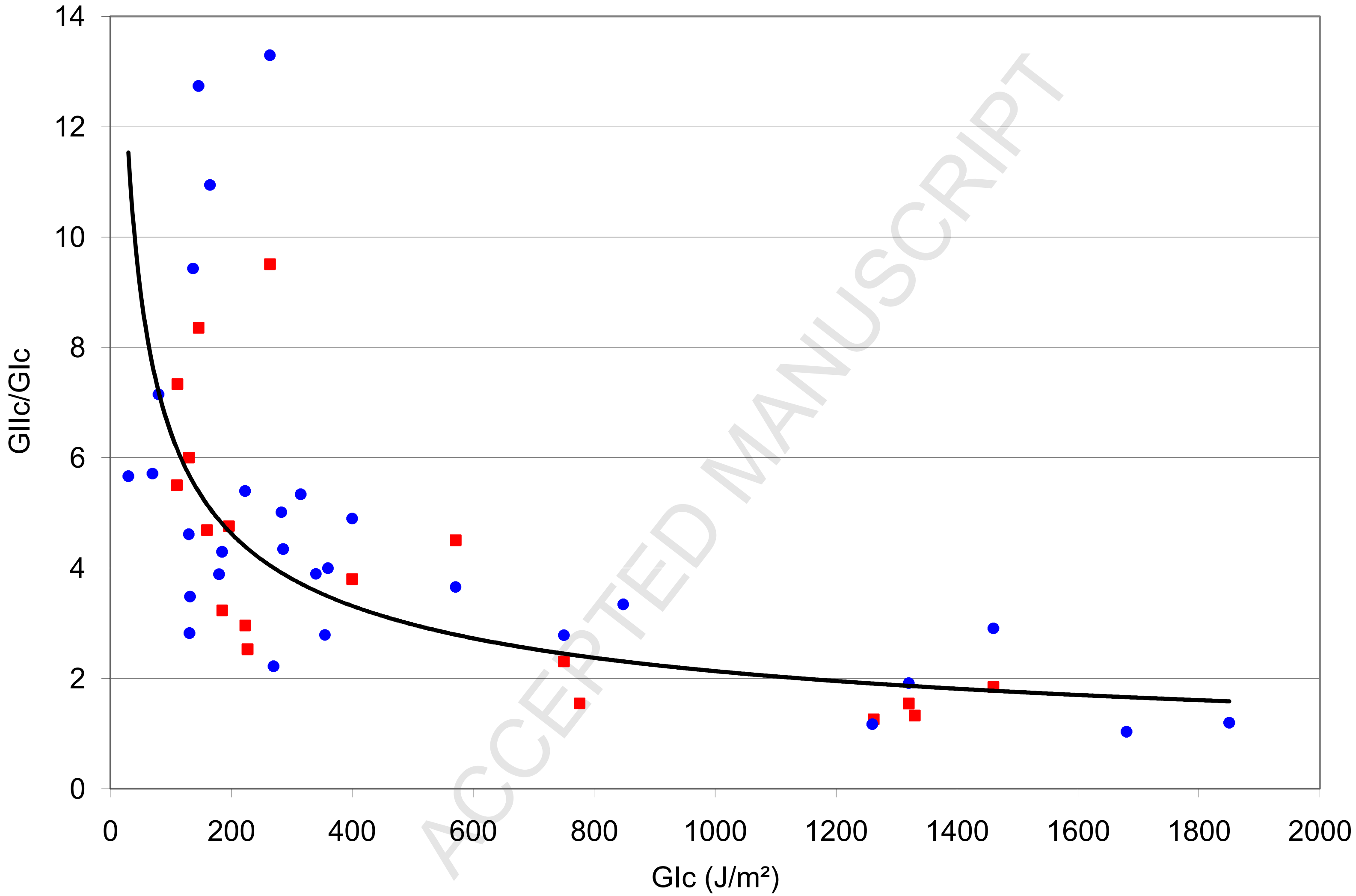

GIIc/GIc
14
12
10
8
6
4
2
0
0
200
400
600
800
1000
1200
1400
1600
1800
2000
GIc (J/m²)

Figure 9a

Figure 9b

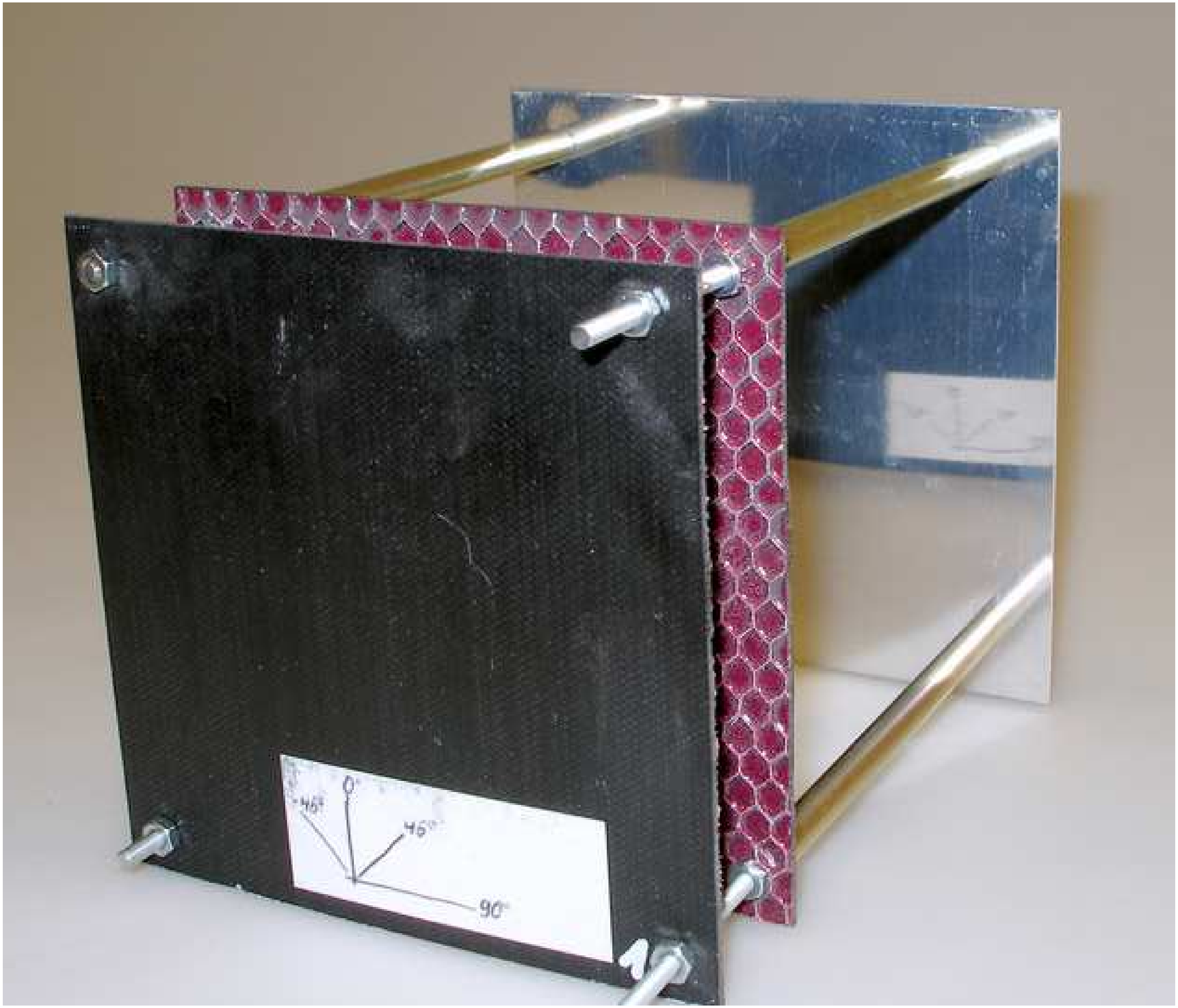

Figure 10

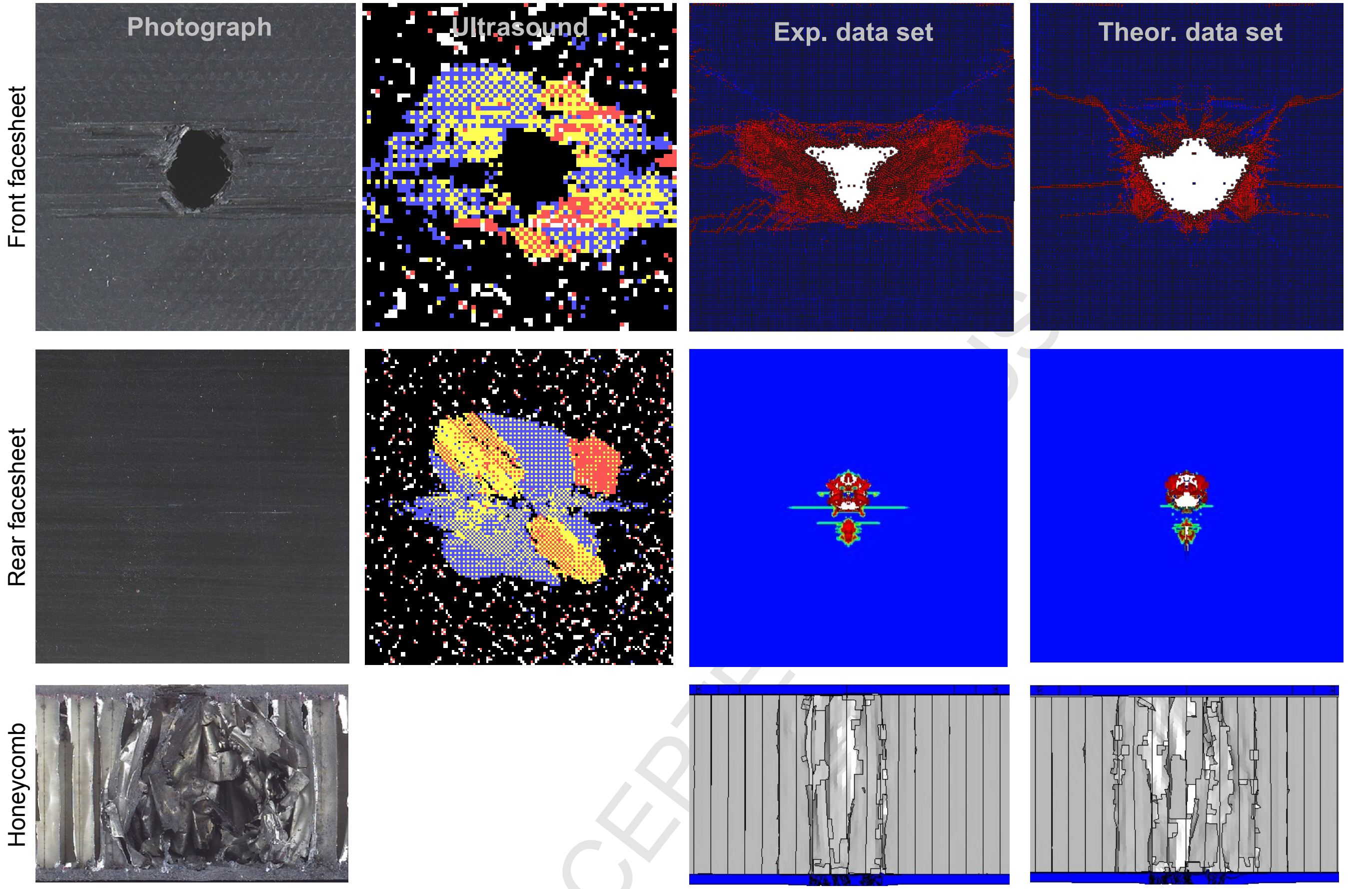
Photograph
Ultrasound
Exp. data set
Theor. data set
Front facesheet
Rear facesheet
Honeycomb

Figure 11

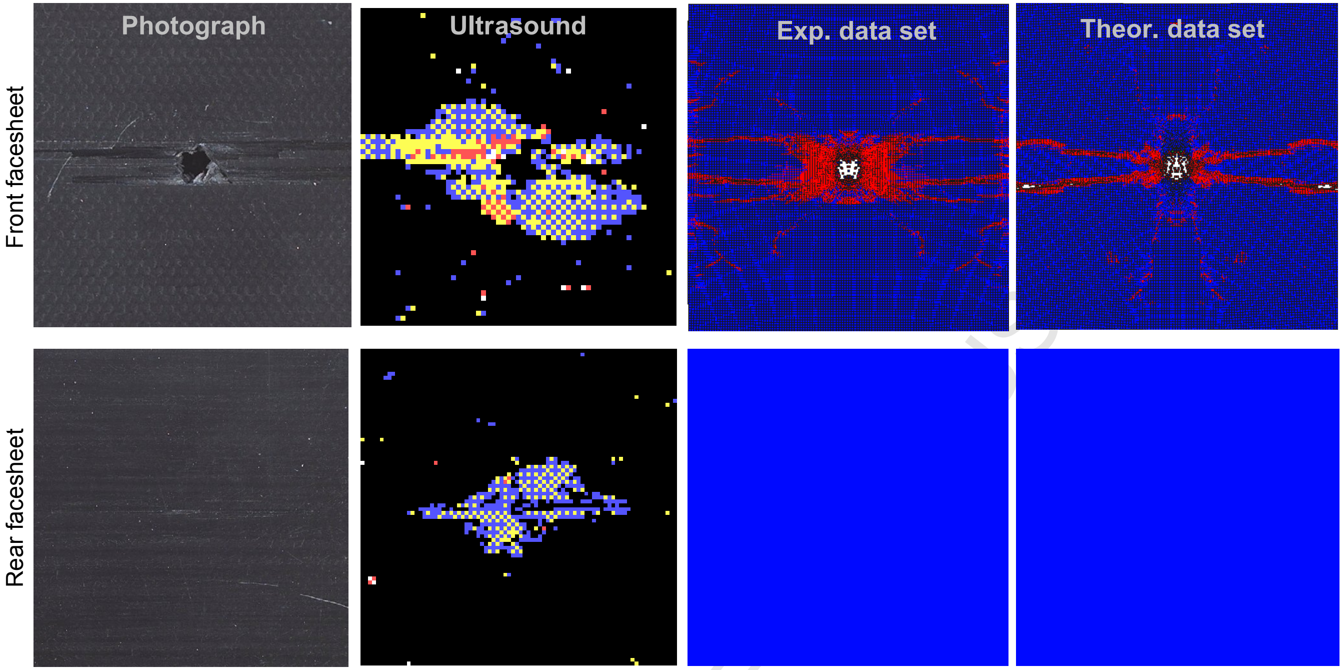
Photograph
Ultrasound
Exp. data set
Theor. data set
Front facesheet
Rear facesheet